CHALMERS

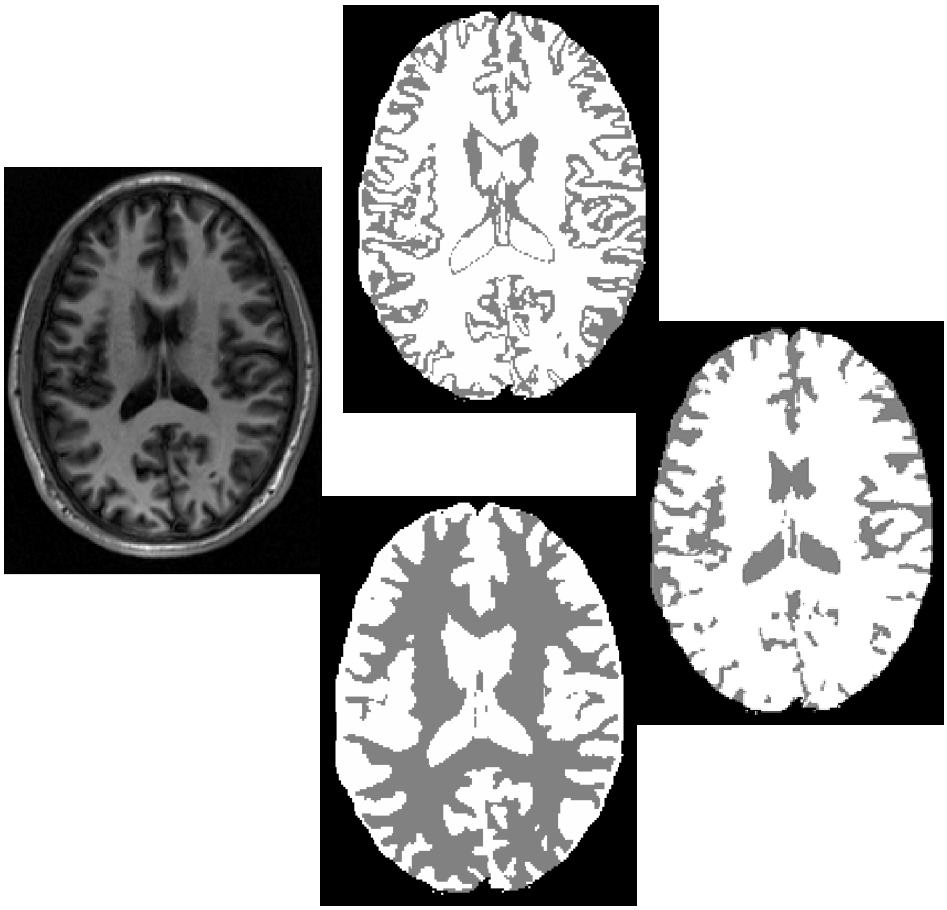

# Brain Tissue Segmentation Using Diffusion Tensor Imaging Data

*Master of Science Thesis*

MOHAMMAD JAVADI

Department of Signals and Systems
*Division of Signal Processing and Biomedical Engineering*
CHALMERS UNIVERSITY OF TECHNOLOGY
Göteborg, Sweden 2013
Report No. EX007/2013

REPORT NO. EX007/2013

# Brain Tissue Segmentation Using Diffusion Tensor Imaging Data

MOHAMMAD JAVADI

Department of Signals and Systems
Division of Signal Processing and Biomedical Engineering
CHALMERS UNIVERSITY OF TECHNOLOGY
Göteborg, Sweden 2013

Brain Tissue Segmentation Using Diffusion Tensor Imaging Data
MOHAMMAD JAVADI



Technical Report No. EX007/2013

Department of Signals and Systems
Division of Signal Processing and Biomedical Engineering
Chalmers University of Technology
SE– 412 96 Göteborg
Sweden
Telephone +46 (0)31–772 1000

Brain Tissue Segmentation Using Diffusion Tensor Imaging Data

MOHAMMAD JAVADI
Department of Signals and Systems
Division of Signal Processing and Biomedical Engineering
Chalmers University of Technology

## ABSTRACT

Accurate brain tissue segmentation is important in the context of neuroimaging, especially for quantitative analysis such as volume measurements. The volumetric analysis of different parts of the brain is useful in assessing progress or remission of various diseases, e.g. the Alzheimer's and epilepsy. The common way to segment brain images is by using structural Magnetic Resonance Imaging (MRI) signals alone such as T1, T2 and proton density. To potentially enhance the brain tissue segmentation the use of additional channels from other MRI techniques could be introduced.

In this thesis we investigate brain tissue segmentation of MR images using Diffusion Tensor Imaging (MR-DTI) data. Three-class problem was studied where the brain volume voxels were classified into one of the three main tissue types: gray matter (GM), white matter (WM), and cerebrospinal fluid (CSF). Different diffusion tensor based features were extracted from the raw DTI data and investigated with respect to discrimination power. In addition, several feature sets were generated by forward selection and backward elimination. The image segmentation was performed using k-means algorithm with a modified combination of bootstrap, cluster center initialization, and early stopping criterion. Different hierarchical classification schemes were evaluated.

The best segmentation results were obtained using the feature set consisting of anisotropy features and one the diffusion tensor eigenvalues, with total class reference based AUC=0.73 (Dice index CSF=0.56, GM=0.67, WM=0.72). The proposed modification of k-means resulted in up to two times faster execution times, compared with the standard k-means algorithm. Using hierarchical classifier led to higher segmentation accuracy compared to the one-step classifier. The developed algorithm could be used for unsupervised brain tissue segmentation. However, to obtain higher segmentation accuracy the fusion with structural MR data may be required.

**Index Terms:** brain tissues, image segmentation, k-means clustering, multi-class classification, magnetic resonance, diffusion tensor imaging

# ACKNOWLEDGEMENT

This master thesis project has been carried out in MedTechWest at Sahlgrenska Hospital, Göteborg. I show my appreciation to all the persons who have contributed to this work especially to:

Prof. Mikael Persson, examiner of the project, for accepting me to carry out my thesis within his research group at MedTechWest.

Dr. Artur Chodorowski, my supervisor for being a great supportive leader and friend. I'm thankful for helping me to perform research in the diffusion tensor imaging field and introducing the evaluation techniques.

Irene Perini, Dan-Mikael Ellingsen, and Dr. Min-Yi Xiao for the medical consultation and assists. Especially to Irene Perini for teaching me the anatomy of the brain and preparing the manual ground truth.

Massoud Shamaizadeh, my friend for drawing Figure 2.3.

# LIST OF ACRONYMS

| | |
|---|---|
| ADC | Apparent Diffusion Coefficient |
| AUC | Area Under ROC Curve |
| CM | Confusion Matrix |
| CSF | Cerebrospinal Fluid |
| DT | Diffusion Tensor |
| DTI | Diffusion Tensor Imaging |
| EPI | Echo Planar Imaging |
| FA | Fractional Anisotropy |
| FN | False Negative |
| FP | False Positive |
| FS | Feature Set |
| GM | Gray Matter |
| GT | Ground Truth |
| MD | Mean of Diffusion |
| MR-DTI | Magnetic Resonance - Diffusion Tensor Imaging |
| MRI | Magnetic Resonance Imaging |
| PD | Proton Density |
| RA | Relative Anisotropy |
| ROC | Receiver Operating Characteristic |
| T1 | T1 Imaging |
| T2 | T2 Imaging |
| TE | Echo Time |
| TN | True Negative |
| TP | True Positive |
| TR | Repetition Time |
| VF | Volume Fraction |
| VR | Volume Ratio |
| WM | White Matter |

**Table of Contents**

**To My Father and Mother**

# 1 INTRODUCTION

## 1.1 Introduction

Segmentation is known as one of the main techniques used for investigation the structure and function of the brain. In segmentation, the objective is to partition the brain volume into a number of predefined tissues. The most common modalities used in brain tissue segmentation are conventional/structural Magnetic Resonance (MR) signals: T1-weighed, T2-weighted, and proton density (PD) [1,2]. An alternative data source is Magnetic Resonance-Diffusion Tensor Imaging (MR-DTI) technique [3,4], which is based on detecting the diffusion of the water molecules in the brain tissues. The ability of the DTI to discern the white matter tracts in the human brain is a basic purpose of the clinical investigations such as white matter fiber tracking [5], tractography of the limbic system [6], schizophrenia diagnosing [7], brain tumor detection [8] and volumetric analysis of cerebrospinal fluid and gray matter. The three tissues, white matter (WM), gray matter (GM) and cerebrospinal fluid (CSF), occupy almost all of the brain volume, thus discrimination of these tissues allows us to extend the brain study to the entire brain.

The use of MR-DTI for brain tissue segmentation purpose is still rare and mostly used for detection of white matter tracts [5-8]. Some studies have included DTI-data for brain tissue segmentation, however only a few features have been used as discriminatory parameters [9]. Therefore there is a need to investigate a larger number of DTI-based features in the context of tissue segmentation and compare with the segmentation results based on structural MR features.

In this work, we focus on brain tissue segmentation using MR-DTI data, where all three major brain tissues including white matter, gray matter, and cerebrospinal fluid are taken into account. As discriminatory parameters we consider twelve DTI-based features extracted from diffusion tensor data (eigenvalues, scalar invariants, relative and fractional anisotropy, volume ratio and fraction, and skewness) and twelve multi-feature sets proposed by feature selection step. As the segmentation method we investigate the k-means clustering algorithm, which belongs to unsupervised learning methods. In the k-means algorithm, the segmentation results are affected by the initial position of the cluster's center-points. Thus to potentially enhance the segmentation results, the original k-means algorithm is modified by introducing a combination of bootstrap and cluster-center initialization. Beside these modifications, to reach the same segmentation accuracy in a shorter time, early stopping criterion is proposed.

## 1.2 Aims and Objectives

The aim of the thesis was to:

1. Develop an unsupervised method for brain tissue segmentation based on diffusion tensor imaging data.
2. Evaluate the performance of the method using synthetic and real clinical data.
3. Compare the DTI-based segmentation with segmentation based on structural magnetic resonance data.

## 1.3 Thesis organization

The thesis is organized as follows. Chapter 2 gives a medical background on human brain, significant parts of the diffusion tensor imaging, and MR modalities. Chapter 3 summarizes previous research works conducted in areas related to the brain tissue segmentation and diffusion tensor imaging. Chapter 4 presents the characteristic of the input data. In Chapter 5 the data analysis and segmentation methods used in the Thesis are presented. The experimental results are shown in Chapter 6 and discussion is conducted in Chapter 7. Finally, Chapter 8 gives the conclusion and suggests future work.

# 2 BACKGROUND

## 2.1 Brain Anatomy

To study the interested brain tissues by MR-DTI data, we need to know about the anatomy of these tissues which are cerebrospinal fluid (CSF), gray matter (GM), and white matter (WM).

CSF is a colorless liquid which surrounds and fills the space in the brain. It supports the brain and maintains pressure in the skull. Also it carries some substances into/out of the brain. CSF is held by four ventricles within the brain (see Figure 2.1) [10].

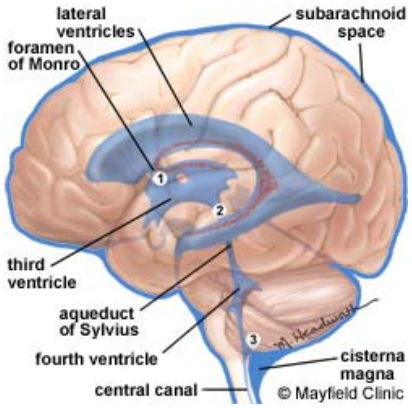


*Figure 2.1: CSF pathway and ventricles of the brain.*

WM and GM are opposing tissues. WM comprises myelinated nerve fibers and is a pathway for signals from one region to another region of the cerebrum also between the cerebrum and lower brain centers. GM comprises both nerve fibers and nerve cell bodies. In Figure 2.2 the WM and GM are denoted [11].

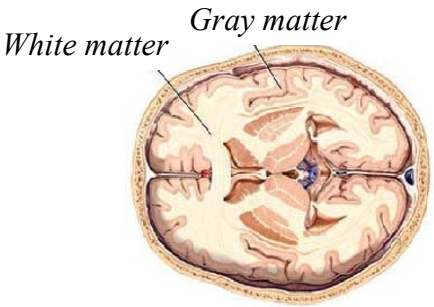


*Figure 2.2: White matter and Gray matter within the brain.*

## 2.2 Diffusion Tensor Imaging

To make the research more understandable the significant parts of the diffusion tensor imaging (DTI) are presented in this section.

### 2.2.1 Diffusion Types

Diffusion of the water molecules is performed in an ellipsoid form. If this diffusivity has the same values for each direction, it is termed diffusion isotropic, otherwise it is termed diffusion anisotropic [12].

The diffusion is characterized by a diffusion tensor matrix with corresponding eigenvalues [13]. In isotropic diffusion all the eigenvalues ($\lambda_1$, $\lambda_2$, $\lambda_3$) are equal in all the directions (i.e. $\lambda_1=\lambda_2=\lambda_3$) and it is spherical form, see Figure 2.3a. An anisotropic diffusion has two common models. In the first model, two eigenvalues are large and the third one is almost zero (e.g. $\lambda_1=\lambda_2$, $\lambda_3\approx 0$) and it is planar form, see Figure 2.3b. The second model is linear form and has one large eigenvalue and the others are almost zero (e.g. $\lambda_3>>\lambda_1=\lambda_2\approx 0$), see Figure 2.4c.

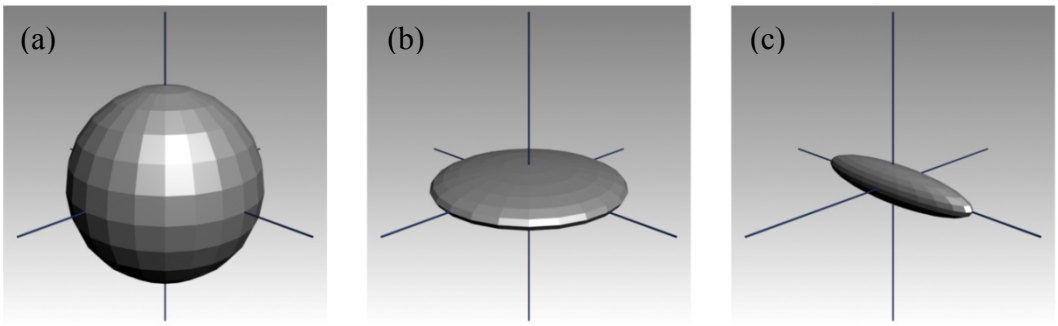


*Figure 2.3: Three diffusion forms: (a) Spherical, (b) Planar, (c) Linear.*

### 2.2.2 Calculating the Diffusion Tensor

In MR-DTI diffusion of the water molecules is calculated for each voxel at several directions. The diffusion value is measured by the Stejskal-Tanner sequence with two strong symmetrical gradient pulses. First gradient pulse causes a phase shift for all the spins. This phase shift is inversed by the second one. Whereas Brownian motion interferes during the time period ($\Delta$), these two phase shifts are not equal. Therefore, the signal is lost, see Figure 2.4 [14]. The dependence of the spin density is eliminated with two independent measurements of diffusion weighted images. One measurement without diffusion weighting and one with diffusion weighting, which are calculated by equation 2.1.

$$S = S_0 e^{-bD} \qquad 2.1$$

where $S_0$ is measurement without diffusion weighting, $S$ is measurement with diffusion weighting, $D$ is a diffusion value in the voxel, and $b$ is the diffusion weighting factor.

The regular used *b* values for the brain studies are in the range of 700 to 1300 s/mm$^2$. Also the most common *b* value is 1000 (s/mm$^2$) [15].

$$b = \gamma^2 \delta^2 \left( \Delta - \frac{\delta}{3} \right) |g|^2 \qquad 2.2$$

where γ is the proton gyro magnetic ratio (42 MHz/Tesla for water proton spin), |g| is the strength (i.e. area) of the diffusion sensitizing gradient pulse with δ duration, and Δ is the time between diffusion gradient pulses [16].

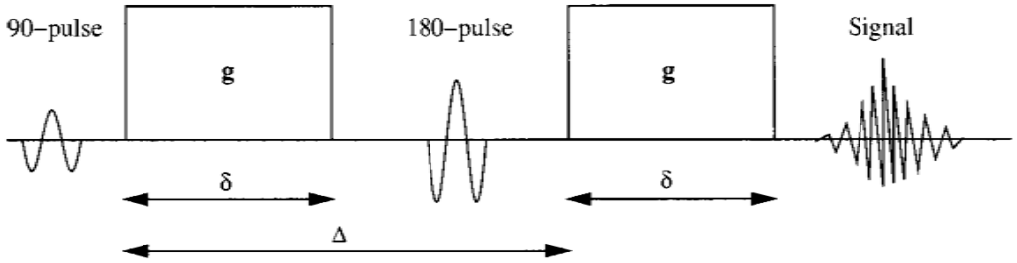


*Figure 2.4: The Stejskal-Tanner sequence.*

For the anisotropic diffusion the equation 2.1 is written in a more general form in equation 2.3.

$$S = S_0 \, e^{-\gamma^2 \delta^2 \left[\Delta - (\delta/3)\right] g^T D g} \qquad 2.3$$

The equation 2.3 is converted to the isotropic form with **D** = D**I** (where **I** is the identity tensor) and normalizing the gradient vectors, $\hat{g} = g / |g|$ in equation 2.4.

$$S = S_0 \, e^{-b \hat{g}^T \mathbf{D} \hat{g}} \qquad 2.4$$

In the typical case, the symmetric 3×3 diffusion tensor **D** has six degrees of freedom. Thus to estimate the tensor at least six measurements are required. For this purpose, seven independent images with different gradient directions and diffusion weightings are prepared. The symmetric 3×3 diffusion tensor **D** is characterized below,

$$D = \begin{bmatrix} D_{xx} & D_{xy} & D_{xz} \\ D_{yx} & D_{yy} & D_{yz} \\ D_{zx} & D_{zy} & D_{zz} \end{bmatrix} \qquad 2.5$$

Anisotropic diffusion in the brain tissues is characterized by the diffusion tensor **D**.

## 2.3 Diffusion Tensor Based Features

Several measures of diffusion anisotropic have been proposed [17-21]. In this project twelve measures/features are used in the subsequent segmentation experiments. These features are presented below.

**a) Eigenvalues ($\lambda_1$, $\lambda_2$, $\lambda_3$)**

These parameters describe how the spherical shape of the eigenvalues ($\lambda_1$, $\lambda_2$, $\lambda_3$) reform to ellipsoid shape.

**b) Ratio of Eigenvalues**

Simple index for detecting the diffusion anisotropic/isotropic is the ratio between the largest and the smallest eigenvalues as the following equation,

$$A_{ratio} = \frac{\lambda_1}{\lambda_3} \qquad \mathrm{A_{ratio}} \geq 1 \tag{2.6}$$

**c) Relative Anisotropy**

$$RA = \frac{1}{\sqrt{6}} \frac{\sqrt{\sum_{i=1,2,3} (\lambda_i - \bar{\lambda})^2}}{\bar{\lambda}} \quad \text{where, } \bar{\lambda} = \frac{1}{3}\sum_{i=1}^{3} \lambda_i \tag{2.7}$$

**d) Fractional Anisotropy**

$$FA = \sqrt{\frac{3}{2}} \sqrt{\frac{\sum_{i=1,2,3} (\lambda_i - \bar{\lambda})^2}{\sum_{i=1,2,3} \lambda_i^{\,2}}} \quad \text{where, } \bar{\lambda} = \frac{1}{3}\sum_{i=1}^{3} \lambda_i \tag{2.8}$$

**e) Scalar Invariants $I_1$ , $I_2$ , $I_3$**

$$I_1 = \lambda_1 + \lambda_2 + \lambda_3 \tag{2.9}$$

$$I_2 = \lambda_1 \lambda_2 + \lambda_2 \lambda_3 + \lambda_3 \lambda_1 \tag{2.10}$$

$$I_3 = \lambda_1 \cdot \lambda_2 \cdot \lambda_3 \tag{2.11}$$

**f) Volume Ratio (VR)**

$$VR = 27\left( I_3 \Big/ I_1^3 \right) \tag{2.12}$$

**g) Volume Fraction (VF)**

$$VF = (I_1^3 - 27I_3) \Big/ I_1^3 \qquad 2.13$$

**h) Skewness of λ**

$$Skew = \frac{\left(\lambda_1 - \bar{\lambda}\right)^3 + \left(\lambda_2 - \bar{\lambda}\right)^3 + \left(\lambda_3 - \bar{\lambda}\right)^3}{3} \qquad 2.14$$

*Table 2.1: Summary of the extracted features.*

| | |
|---|---|
| **Eigenvalues** | $\lambda_1$ , $\lambda_2$ , $\lambda_3$ |
| **Ratio of Eigenvalues** | $A_{ratio} = \lambda_1 \Big/ \lambda_3 \qquad A_{ratio} \geq 1$ |
| **Relative Anisotropy** | $RA = \frac{1}{\sqrt{6}} \frac{\sqrt{\sum_{i=1,2,3} (\lambda_i - \bar{\lambda})^2}}{\bar{\lambda}}$ |
| **Fractional Anisotropy** | $FA = \sqrt{\frac{3}{2}} \sqrt{\frac{\sum_{i=1,2,3} (\lambda_i - \bar{\lambda})^2}{\sum_{i=1,2,3} \lambda_i^2}}$ |
| **Scalar Invariants $I_1$ , $I_2$ , $I_3$** | $I_1 = \lambda_1 + \lambda_2 + \lambda_3$<br>$I_2 = \lambda_1 \lambda_2 + \lambda_2 \lambda_3 + \lambda_3 \lambda_1$<br>$I_3 = \lambda_1 \cdot \lambda_2 \cdot \lambda_3$ |
| **Volume Ratio** | $VR = 27\left(I_3 \Big/ I_1^3\right)$ |
| **Volume Fraction** | $VF = (I_1^3 - 27I_3) \Big/ I_1^3$ |
| **Skewness of λ** | $Skew = \frac{\left(\lambda_1 - \bar{\lambda}\right)^3 + \left(\lambda_2 - \bar{\lambda}\right)^3 + \left(\lambda_3 - \bar{\lambda}\right)^3}{3}$ |

## 2.4 MRI Modalities

The conventional Magnetic Resonance Imaging (MRI) [22,23] is another type of imaging. Different contrasts of the deep tissues in vivo are used to quantify and localize the tissues by MRI.

Three types of MR imaging are defined as T1, T2, and Proton Density (PD). The principles of generating the T1, T2, and PD are based on the behaviors of different molecules (specifically water and fat molecules) within the echo time ($T_E$) and relaxation time ($T_R$). These MRI modalities are illustrated below.

### 2.4.1 T1 Modality

In T1 imaging the $T_R$ and $T_E$ times have short period. The relaxation of fat molecules is even faster than that in water molecules. Thus in the short $T_E$ period, almost all the fat molecules align with the static magnetic field. However, the water molecules are unable to perform that. Therefore, the fat molecules generate more radio frequency signals than the water molecules and the obtained image has brightness at the fat and darkness at the other regions [22].

Figure 2.5 shows T1 image; it is seen WM is brighter than CSF; and contrast of GM is in the middle of these two regions.

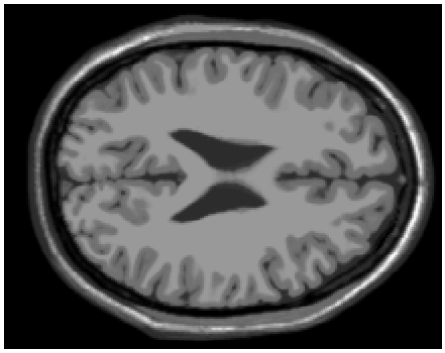

*Figure 2.5: T1 image.*

### 2.4.2 T2 Modality

In T2 imaging the $T_R$ and $T_E$ times have long period. Thus within the long relaxation period both of the fat and water molecules have enough time to align with static magnetic field. In total the generated radio frequency signals by the water molecules have higher values than the fat molecules. Thus the obtained image is bright at the water and dark at the other regions [22].

Figure 2.6 shows T2 image; it is seen CSF is brighter than WM; and contrast of GM is in the middle of these two regions.

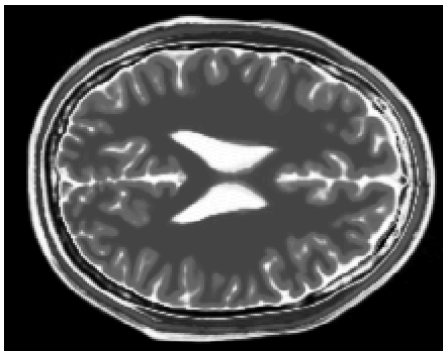

*Figure 2.6: T2 image.*

### 2.4.3 Proton Density Modality

In this type of imaging, the data acquisition from differences in the amount of available spins (hydrogen nuclei in water) with short $T_E$ and long $T_R$, is carried out. The spin of water molecule is higher than that in fat molecule. Thus in short $T_E$ the water molecules have more spins than fat molecules. Within the long relaxation period both of the fat and water molecules have enough time to align with static magnetic field. However, the water molecules have more spins and generate more radio frequency signals than the fat molecules [22]. Because of the short $T_E$ the radio frequency signals of the water and fat molecules are close. Thus the contrast between the fat and water regions is low.

Figure 2.7 shows PD image is brighter in the fat region (WM) in comparison with T2 image (Figure 2.6); and it is brighter in water region (CSF) in comparison with T1 image (Figure 2.5).

*Figure 2.7: PD image.*

# 3 LITERATURE REVIEW

Diffusion tensor imaging is mostly used for tractography of neural tracts [24-26] and few research projects have been carried out for the brain tissue discrimination. In what follows some of the reported research projects on DTI and tissue discrimination are reviewed.

Bazin *et al.* (2009) investigated the WM tracts on DTI data. Markov Random Field (MRF) was proposed to model the diffusion properties [27]. In addition the belief propagation technique was used to estimate the WM tracts in each voxel. Several datasets from an atlas, five healthy subjects, and seven multiple sclerosis patients were used. In the evaluation of the algorithm on ten atlas images and nine major tracts, the authors report the DSI values ranging from 0.32 to 0.73. The highest DSI value was reported for the cortico-spinal tract (CST).

Cai *et al.* (2006) carried out another research [28]. The study was conducted on 18 MRI brain datasets. Cai investigated 15 brain tissue structures (nine GM and six CSF structures). The segmentation was performed by Narrowband Level Set and pattern classification methods based on maximum a posteriori (MAP) probability framework. The results were evaluated by the gold standards which provided by expert radiologists. The obtained mean DSI value for the ventricle structures (CSF) was over 0.70 and for the GM structures was over 0.60.

Han *et al.* (2009) performed an investigation to discriminate the CSF, WM, and GM tissues [29]. Han used three segmentation methods/tools: graph-cuts, FSL-FAST tool, and thresholding. Segmentation was performed on ten real DTI data and the results were compared with manual segmentation which had been done by a physician expert. In the segmentation procedure, at the first step the CSF/non-CSF regions were discriminated from the third eigenvalue ($\lambda_3$). Then the discriminated CSF regions were masked from the fractional anisotropy (FA) feature. Then after the obtained data were segmented into the WM and GM (non-WM). The mean DSI values were CSF= 0.88, GM= 0.77, and WM= 0.90.

Liu *et al.* (2007) did another research to discriminate WM, GM, and CSF tissues [30]. The segmentation was performed on ten DTI data. The Expectation-Maximization (EM) algorithm was combined with Hidden Markov Random Field model (HMRF) to perform the WM/non-WM and CSF/non-CSF classifications. For CSF discrimination Apparent Diffusion Coefficient (ADC) and three eigenvalues ($\lambda_1$, $\lambda_2$, $\lambda_3$) were used; also WM tissue was discriminated by these features: FA, relative anisotropy (RA), and

volume ratio (VR). In this study the CSF/non-CSF regions were obtained from the ADC and three eigenvalues. Also the WM/non-WM regions were obtained from FA, RA, and VR features. The Simultaneous Truth and Performance Level Estimation (STAPLE) algorithm was utilized to estimate the combination of the discriminated regions to discern CSF, WM, and GM tissues. As a final results the obtained DSI values were CSF= 0.61, GM= 0.88, and WM= 0.90.

The reviewed articles are summarized in Table 3.1.

*Table 3.1: Overview of selected articles.*

| Author and Title | Year | Methods | Results (DSI) |
|---|---|---|---|
| Bazin *et al.*<br>Belief Propagation Based Segmentation of White Matter Tracts in DTI [27] | 2009 | - Belief Propagation<br>- Markov Random Field (MRF) | CST= 0.73<br>(WM tract) |
| Cai *et al.*<br>Evaluation of Two Segmentation Methods on MRI Brain Tissue Structures [28] | 2006 | - Narrow Band Level Set Method<br>- Pattern classification method based on maximum a posteriori (MAP) | CSF= 0.70<br>GM= 0.60 |
| Han *et al.*<br>An Experimental Evaluation of Diffusion Tensor Image Segmentation Using Graph-Cuts [29] | 2009 | - Graph-cuts,<br>- FSL-FAST tool<br>- Thresholding | WM= 0.90<br>GM= 0.77<br>CSF= 0.88 |
| Liu *et al.*<br>Brain Tissue Segmentation Based on DTI data [30] | 2007 | - Expectation Maximization (EM)<br>- Hidden Markov Random Field (HMRF) | WM= 0.90<br>GM= 0.88<br>CSF= 0.61 |

The results reported in the above reviewed articles are compared with the experimental results of the present project in Chapter 6.

# 4 MATERIAL

## 4.1 Input Data

In the segmentation experiments two types of datasets were used:

Dataset 1: real data and Dataset 2: simulated data

**Dataset 1: real data,** DTI and T1 modality

These data have been gathered at the Sahlgrenska University Hospital at Göteborg from a healthy person (30-year) with these details:

**DTI data:** {Size: 128×128×56, Number of Directions: 15, Technique: DwiSE, by Philips instrument, Maximum Diffusion *b* value: 1000 (s/mm$^2$)}

*Figure 4.1: DTI image, third eigenvalue ($\lambda_3$), axial layer #90.*

**T1 data:** {Size: 256×256×196, Voxel volume: 1 mm$^3$, Philips instrument: 1 Tesla Scanning Sequence: 'GR', Color Type: 'grayscale'}

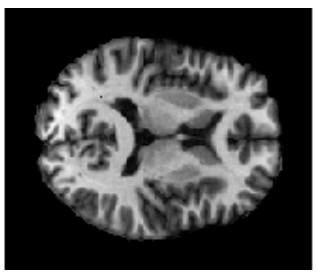

*Figure 4.2: Real T1 Image, axial layer #90.*

**Dataset 2: simulated data,** T1, T2, and PD modalities

These data have been collected from the Brainweb site [31]. The data with the following specifications were used in the experiments: 1mm slice thickness, brain volume size 181×217×181 voxels, zero noise level, and zero intensity non-uniformity.

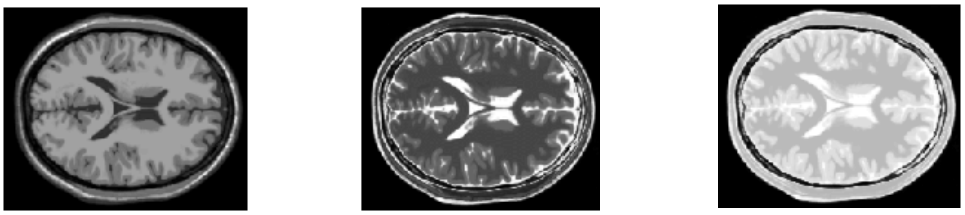

*Figure 4.3: Simulated data from left to right are: T1, T2, and PD.*

## 4.2 Ground Truth

A reference or ground truth (GT) segmentation for each dataset was obtained as follows. For Dataset 1, an experienced physician, manually segmented the data into the three tissue classes: CSF, GM, and WM. For Dataset 2, the ground truth was obtained from the nine tissue classes defined in the synthetic data. The used labels for the three classes were: cerebrospinal fluid, gray matter, and white matter. The obtained ground truth segmentations, were used in the performance evaluation of the segmentation algorithms.

## 4.3 Data Format

The MRI data have several protocols/formats: NIFTI, DICOM, and MINC which are briefly illustrated below.

**NIFTI.** This protocol is focused on fMRI but the other MR instruments use it as well [32]. NIFTI stands for Neuroimaging Informatics Technology Initiative. The file extension in this format is *nii*. The real DTI data in the current study, are in this format.

**DICOM.** The data acquisition from the MRI instrument is in this format. The file extension in this format is *dcm* [33]. DICOM stands for Digital Imaging and Communications in Medicine. The real T1 data in the current study, is in this format.

**MINC.** This data format was especially designed for the medical imaging. The file extension in this format is *mnc* [34]. The simulated data in this study, are in this format.

**Data Conversion.** The three above mentioned formats can be converted to each other by suitable software or Matlab functions. The collected original data in this project are in three formats: NIFTI, MINC, and DICOM. The NIFTI format was selected as the common format; and all the brain data volumes were converted to this format. In the conversion process the MINC file was converted to NIFTI using *mnc2nii* program. Also for converting the DICOM to NIFTI, software of *Chris Rorden Company* [35] was used.

# 5 METHODS

## 5.1 Brain Volume Preprocessing

In the current project the following preprocessing were applied:

**Diffusion matrix extraction.** The DTI probes the diffusion properties of water molecules in tissues such as magnitude, direction, and anisotropy. These data are collected from different directions by DT-MRI and gathered in several brain volumes. The collected data cannot be engaged directly in the segmentation procedure and data preprocessing, to extract the diffusion matrix (D-matrix), is required. The procedure was performed using FSL's FDT tool as follows [36]:

- **Eddy current correction.** The MR-DTI works with high magnetic field. Therefore, during the brain imaging eddy current is induced within the tissues. Thus image reconstruction gets distortion geometrically and the image is blurred. For this reason, at the first step, this artifact was removed from the data.

- **Brain extraction.** Brain tissues were interested in this project thus the skull was removed by the FSL Brain Extraction Tools (BET).

- **Construct diffusion tensors.** In this process from all the gathered brain volumes, one brain volume was extracted in which each voxel was characterized with a D-matrix [36].

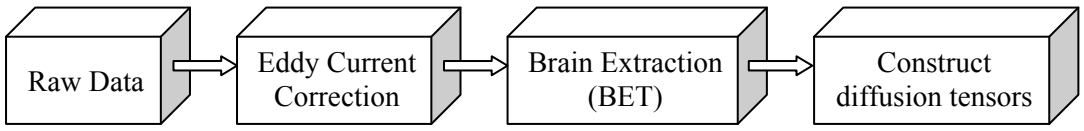


*Figure 5.1: FSL's FDT Tool process for D-matrix extraction from the raw DTI data.*

**Registration.** Another applied preprocessing procedure is registration. In this project to evaluate the results of the DTI segmentation, ground truth obtained from the T1 image of the brain. To have possibility to compare DTI and T1 data, these data need to overlap as best possible. Thus to align the DTI image on T1 image (GT), DTI data was registered with T1 data by FSL's FLIRT tool [36].

## 5.2 Feature Extraction

The feature extraction is significant part of the project. As mentioned before by the help of FDT-FSL tool, three eigenvalues ($\lambda_1$, $\lambda_2$, $\lambda_3$) were extracted. These eigenvalues values were used to measure the other features such as mean of diffusion ($\bar{\lambda}$), fractional anisotropy (FA), relative anisotropy (RA), volume ratio (VR), volume fraction (VF), scalar invariants ($I_1$, $I_2$, $I_3$), and skewness of $\lambda$ (Skew), based on the mentioned formulas in Chapter 2 (equations 2.6 to 2.14).

## 5.3 Feature Normalization

The feature normalization can be done in different ways [37]. Within this project the data values were normalized into [0, 1] interval according to equation 5.1.

$$NF = \frac{F - F_{min}}{F_{max} - F_{min}} \qquad 5.1$$

where: $NF$ is normalized feature, $F$ is original feature value,
$F_{min}$ is the minimum feature value, and $F_{max}$ is the maximum feature value.

## 5.4 Feature Selection

The main idea behind the feature selection is, choosing a subset of the features which has more influence on discrimination of interested tissues. The advantages of feature selection are such as reducing the dimension of the feature space which may speed up the segmentation procedure, improving the results' quality, and keeping the relevant features. Feature selection methods and fundamental algorithms are presented below.

### 5.4.1 Forward Selection and Backward Elimination Methods

There are two major methods for feature selection: forward selection and backward elimination.

**Forward Selection.** It begins with choosing the variables one by one with respect to decrease the feature selection criterion the most. The process is terminated when addition of variable does not significantly decrease the criterion [38].

**Backward Elimination.** The process is started with all the variables and attempts to eliminate the variables one by one with respect to decrease of the criterion. The process is ended when elimination of variable does not significantly decrease the criterion [38].

### 5.4.2 Feature Selection Criterions

Feature selection procedure was performed using the following criterions, implemented in the Pattern Recognition Tools package (PRTools) [39]:

- Minimum of estimated Mahalanobis distances (mMaha)
- Sum of estimated Mahalanobis distances (sMaha)
- Minimum of squared Euclidean distances (mEucl)
- Sum of squared Euclidean distances (sEucl)

## 5.5 Segmentation Methods

In the current project the segmentation was performed using k-means clustering algorithm. The standard k-means method was run with different centroid initializations and stopping criterion values. We call this variant as modified k-means. In the following we give a description of the standard k-means algorithm and our modifications.

### 5.5.1 Standard k-means clustering algorithm

The k-means clustering algorithm is an iterative unsupervised clustering algorithm. The main idea of this algorithm is to define *K* centroids, one for each cluster. The algorithm attempts to place the centroids as much as possible far away from each other. As it was mentioned the k-means with different centroid initializations and stopping criterion values, is used which we call *standard* and *modified k-means*.

The standard k-means clustering algorithm is formulated as follows [40]:

A dataset of *n* observations is assumed $S=\{X_1, X_2, \ldots, X_n\}$; each one is *p*-dimensional. This dataset is going to be divided into *K* sets of clusters: $C_1, C_2, \ldots, C_K$. The objective function to be minimized is,

$$O_K = \sum_{i=1}^{n} \sum_{k=1}^{K} (X_i - \mu_k)^T (X_i - \mu_k) \qquad 5.2$$

where:

$(X_i - \mu_k)^T$ is transpose of matrix $(X_i - \mu_k)$,

$X_i \in S$, $i=1,\ldots n$, and $k=1,\ldots, K$

$\mu_k = \frac{1}{n_k} \sum_{i \in C_k} X_i$ is the mean vector of objects from $C_k$

$n_k$: number of objects in $C_k$

The following steps are involved in the process of finding minimum value of the objective function in equation 5.2:

1) Initialization. *K* objects from dataset are randomly selected. These objects represent initial group of centroids (in this project, K=3).

2) Clustering. Each object is assigned to the group that has the closest centroid. For this purpose the following equation was fulfilled at each iteration *i*,

$$\left\| X_j - \mu_k^{(i)} \right\| = \min \qquad 5.3$$

where: *j = 1, ..., n* and *i: iteration number* *Note: sign* $\| \ \|$ *is the norm*

3) Updating. When all objects were grouped, the centroids are updated with the following equation,

$$\mu_k^{(i)} = \frac{1}{\left| C_k^{(i)} \right|} \sum_{j \in C_k^{(i)}} X_j \quad \forall k \in \{1, 2, \ldots, K\} \qquad 5.4$$

4) Termination. Steps 2 and 3 are repeated until the centroids no longer move.

### 5.5.2 Modified k-means clustering algorithm

The standard k-means clustering algorithm is modified into the modified k-means clustering algorithm by changing the initialization and stopping criterion.

#### 5.5.2.1 Initialization

The k-means clustering algorithm is an iterative method for dividing a dataset into *K* set of clusters and trying to shift the initialization centroids into the local optimal point. Therefore, the optimal segmentation is influenced by the initialization centroids [41]. Regarding to the investigations which have been performed with different initialization methods in [40], bootstrap method gave better results. Therefore, the bootstrap method was selected in this project. It consists of the following steps [42]:

1- Dataset is divided into several subsets (in this project the dataset was divided into four subsets).
2- The segmentation on each subset is performed. In this part the initialization centroids are selected by cluster center initialization which is explained in next section.
3- The last centroids of the subsets are chosen.
4- Initialization centroids for the final clustering step (step 2, section 5.5.1) are selected from the centroid set in step 3 (in this project K=3 thus three distant initialization points are selected).

#### 5.5.2.2 Cluster Center Initialization

Cluster center initialization method is a method to clarify the dense centers of the datasets. These dense centers are considered as the initialization points. Corresponding to the number of clusters, the dense centers are selected (e.g. in this project three dense centers are picked up from the dataset). The procedure is explained below [41]:

1. It is assumed that the dataset has normal distribution.
2. The mean ($\mu$) and standard deviation ($\sigma$) of dataset are computed.
3. The area under the normal curve is computed with the following formula.
   $A= (2s-1)/(2K)$ where: $s=1, 2,..., K$ and $K$ is number of clusters
4. The z value corresponding with $A$ is calculated.
   Since in this project there is a three-class problem (K=3). The percentiles $z_1$, $z_2$, and $z_3$ is computed in a way that the area under the normal curve from:
   - $-\infty$ to $z_1$ is equal to 1/6 *(i.e. $z_1 = - 0.9672$)*
   - $-\infty$ to $z_2$ is equal to 1/2 *(i.e. $z_2 = 0$)*
   - $-\infty$ to $z_3$ is equal to 5/6 *(i.e. $z_3 = 0.9672$)*
5. The dense centers are computed by $x_i = \mu + \sigma z_i$ where: $i=1,...,K$.

#### 5.5.2.3 Stopping criterion

The second modification was carried out on the stopping criterion. According to our experiences, to terminate the segmentation procedure, it is not necessary to obtain equal objective function values for two consecutive iterations. However, it is good enough that the difference of these objective functions become smaller than a stopping criterion value. In this manner, the execution time of the segmentation is decreased. Therefore, selecting a stopping criterion to fulfill both accuracy and execution time is important.

## 5.6 Hierarchical and Non-hierarchical Classifier

The three-class problem in this study can be solved by different segmentation schemes. Here two schemes have been investigated: hierarchical classifier and one-step classifier.

**Hierarchical classification scheme.** The segmentation procedure is performed in several steps. At first brain tissues are segmented into WM/non-WM. Then non-WM is segmented into CSF and GM (non-CSF), see Figure 5.2.

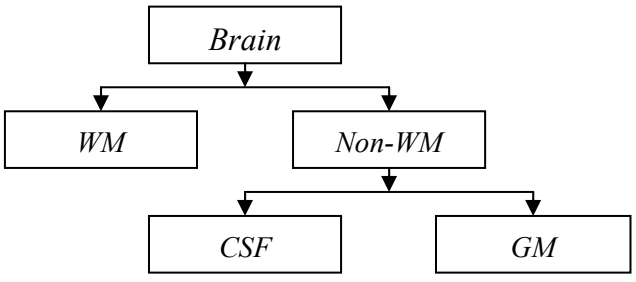


*Figure 5.2: Hierarchical two-stage classification scheme.*

**One-step classification scheme.** In this scheme, the classification is performed in one-step and the image is segmented into *K* cluster at once, see Figure 5.3.

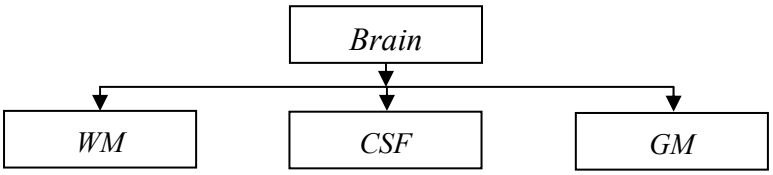


*Figure 5.3: One-step classification scheme.*

## 5.7 Segmentation Performance Evaluation Methods

To evaluate the segmentation results, the following segmentation performance measures were used: confusion matrix (CM), dice similarity index (DSI), ROC curve, Multi-class ROC graph, and Multi-class AUC.

### 5.7.1 Confusion Matrix

The confusion matrix (CM) is a square matrix which is obtained by comparing the segmented data with reference/ground truth. The rows and columns of CM have been named with the same hierarchy. Each column, represents the instances in predicted class and each row, represents the instances in actual class [43]. In the CM the values on the main diagonal represent correct classification while the off-diagonal values represent misclassifications. Thus as much as the density of the values is concentrated on the main diagonal, the segmentation results are more accurate. Figure 5.4 shows an example of a 2×2 CM.

| | | **Actual Value** | |
|---|---|---|---|
| | | **p** | **n** |
| **Prediction Outcome** | **p** | True Positive (TP) | False Positive (FP) |
| | **n** | False Negative (FN) | True Negative (TN) |

*Figure 5.4: Confusion matrix for two-class classifier.*

### 5.7.2 Dice Similarity Index

Dice similarity index (DSI) is a similarity measure over sets [44]. The maximum DSI value is one which corresponds to a perfect segmentation. It is obtained from the CM by the following equation.

$$DSI = \frac{2TP}{2TP + FP + FN} \qquad 5.5$$

### 5.7.3 ROC Curve

Receiver Operating Characteristic (ROC) curve is a graphical plot of the false positive rate (FP) versus true positive rate (TP). The FP and TP values are plotted on the X-axis and Y-axis respectively. The best results correspond to high TP value and low FP value which on the ROC curve, these points are placed on the top left corner [45].

In Figure 5.5 number of operating points are depicted on the ROC curve and the most accurate result is represented by a blue circle.

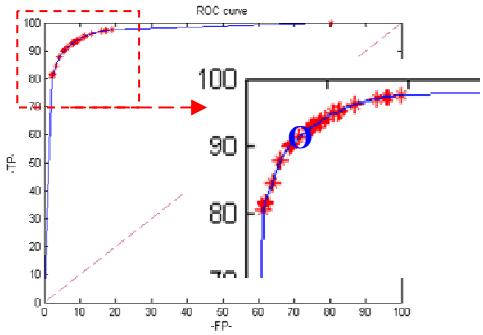


*Figure 5.5: ROC curve and The most accurate point (blue circle).*

### 5.7.4 Multi-class ROC Graph

The multi-class ROC graph, changes n×n CM into the number of 2×2 CMs depending on the number of possible pairs. Then each pair of the objects (2×2 CMs) in the form of a ROC curve, is sketched. This process is performed for all the possible pairs [45]. Since in this project a three-class problem is investigated three-class ROC graph is required. Where a 3×3 CM is generated and turned into three 2×2 CMs as follows:

$$CM = \begin{bmatrix} a_{11} & a_{12} & a_{13} \\ a_{21} & a_{22} & a_{23} \\ a_{31} & a_{32} & a_{33} \end{bmatrix}$$

*The 3×3 CM is turned into three 2×2 CMs: CM1, CM2, and CM3*

$$CM1 = \begin{bmatrix} a_{11} & a_{12} + a_{13} \\ a_{21} + a_{31} & a_{22} + a_{23} + a_{32} + a_{33} \end{bmatrix}$$

$$CM2 = \begin{bmatrix} a_{22} & a_{21} + a_{23} \\ a_{12} + a_{32} & a_{11} + a_{13} + a_{31} + a_{33} \end{bmatrix}$$

$$CM3 = \begin{bmatrix} a_{33} & a_{31} + a_{32} \\ a_{13} + a_{23} & a_{11} + a_{12} + a_{21} + a_{22} \end{bmatrix}$$

Each of the above 2×2 CMs is sketched based on ROC curve's rule and three points are obtained. Therefore, for each 3×3 CM or three-class problem, three points are obtained.

### 5.7.5 Multi-class AUC

The discriminability of a pair of classes is assessed by the Area Under ROC Curve (AUC). In the multi-class problem for each pair, an AUC value is obtained and the total AUC value is calculated by the following equation [45].

$$AUC_{total} = \sum_{c_i \in C} AUC(c_i)\, p(c_i) \qquad 5.6$$

where $AUC(c_i)$ is the area under the class reference ROC curve for class $c_i$ also $p(c_i)$ is the reference class's prevalence in the data:

$$p(c_i) = \frac{\sum_{j=1}^{n} a_{ji}}{\sum_{i=1}^{n}\sum_{j=1}^{n} a_{ji}}$$

$a_{ji} \in$ *CM (confusion matrix)*

*n:* total number of classes
(in this project n=3)

Maximum possible AUC value is one and the AUC may be judged as follows [46]:

- ***Fair;*** when AUC value is higher than 0.70.
- ***Good;*** when AUC value is higher than 0.80.
- ***Excellent;*** when AUC value is higher than 0.90.

# 6 EXPERIMENTAL RESULTS

In this Chapter the data analysis and segmentation results obtained from two datasets which are: (1) DTI-volume from a real patient (2) MR-volume from the simulated brain.

In DTI-volume we did not have access to the ground truth (GT) of the whole real brain volume. Thus the segmentation experiments were carried out on seven slices which were manually segmented by an expert physician. However, in simulated brain we had access to GT for the whole brain.

## 6.1 Feature Extraction and Feature Selection

In the feature extraction procedure, twelve univariate features from DTI raw data were extracted (according to the equations 2.6 to 2.14). Also the feature selection led to the twelve multi-feature sets, obtained from the univariate features.

Table 6.1 shows the results of the feature selection procedure. The feature selection criterions were applied to select the best feature sets for different classification schemes. In the experiments, tissue labels from the expert ground truth were used.

*Table 6.1: The results of the feature selection by different methods.*

| No. | Feature Set (FS) | Criterions | Goodness | Classifier |
|---|---|---|---|---|
| 1 | RA, $\lambda_1$, $\lambda_3$, Skew, $\lambda_2$ | sMaha | GM (72.84) | One-step |
| 2 | FA, $\lambda_1$, $\lambda_2$, I1, Skew | mMaha | GM (72.90) | |
| 3 | FA, RA, $\lambda_1$, I3 | sEucl | CSF (73.35) | |
| 4 | FA, $\lambda_1$, $\lambda_3$, I2 | mEucl | WM (66.91) | |
| 5 | FA, I1 | sEucl | WM (69.18) | Wm/ non-Wm |
| 6 | FA, RA, $\lambda_3$ | mEucl | WM (76.12) | |
| 7 | $\lambda_3$, Skew, $\lambda_2$, FA, I1 | Mahas | WM (72.33) | |
| 8 | $\lambda_3$, Skew, $\lambda_2$, FA, I1, I2, I3 | mMaha | WM (68.56) | |
| 9 | $\lambda_3$, I2, I1, I3, $\lambda_1$ | sEucl | WM (67.16) | |
| 10 | FA, RA, $\lambda_3$, I3 | sMaha | GM (73.15) | CSF/ non-CSF |
| 11 | FA,VR, $\lambda_3$, $\lambda_1$, RA, I3 | mMaha | GM (78.58) | |
| 12 | FA, RA, $\lambda_1$, VR | mEucl | CSF (74.16) | |

For the three-class problem, the best subset was selected by “sEucl” (sum of the Euclidian distances) criterion and resulted in a 4-element dataset: FS4= {FA,RA,$\lambda_1$,I3}.

For discrimination between WM and non-WM the subset was selected by "mEucl" (minimum Euclidian distances) criterion. The suggested dataset contained three features: FS6= {FA, RA, $\lambda_3$}. Finally, for CSF vs. non-CSF tissue, the best dataset containing six elements was obtained by "mMaha" (mean of the Mahalanobis distance) criterion: FS11= {FA, VR, $\lambda_3$, $\lambda_1$, RA, I3}.

## 6.2 Visualization of Input Feature

From the DTI raw data more than ten univariate features were extracted. The selected univariate features of one axial layer (layer #85) are presented in Figure 6.1.

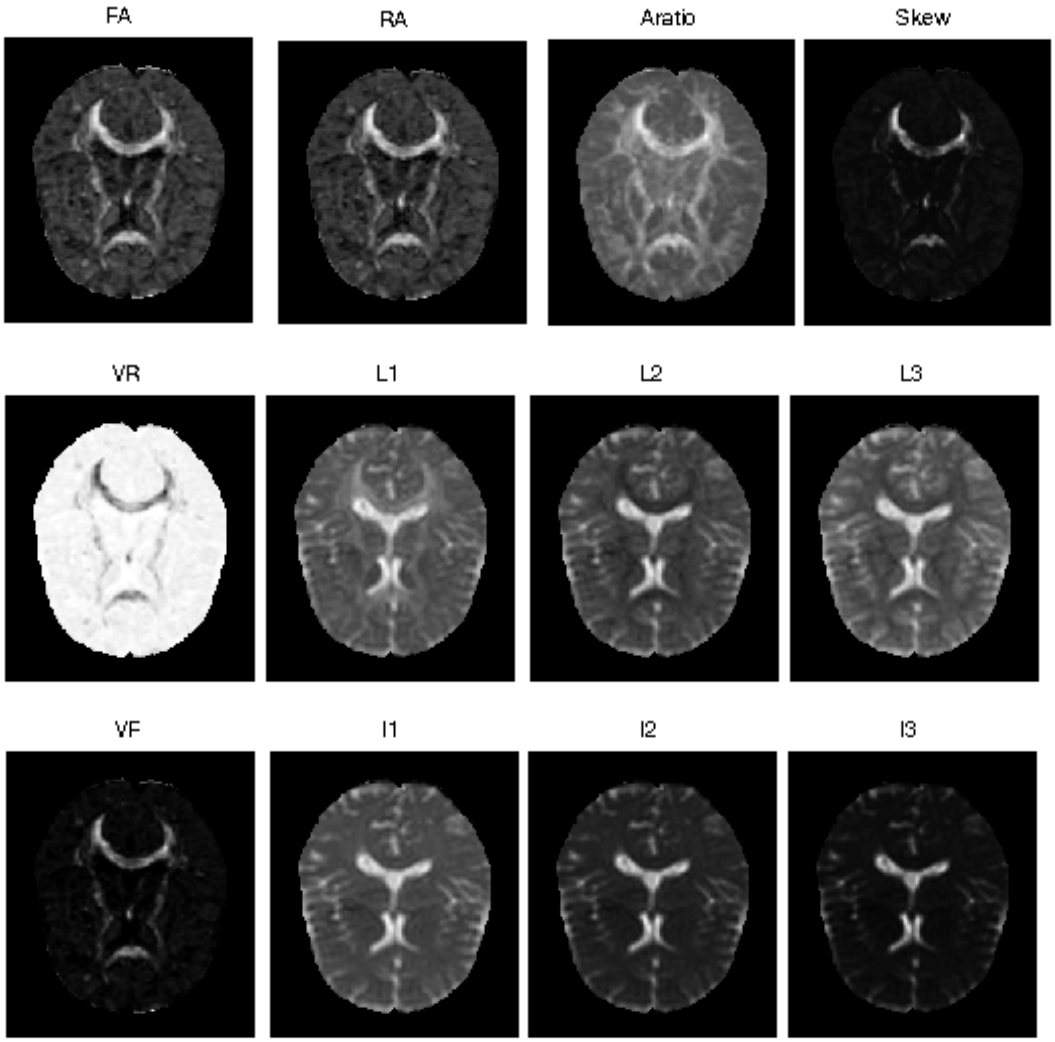


*Figure 6.1: Selected input features, axial layer #85,*
*the features' names are mentioned at the top of the images*

## 6.3 Data Analysis

In this section, discrimination and distribution of the input data are investigated using scatterplots and density functions.

### 6.3.1 Scatterplots

In Figure 6.2 we present the scatterplots for pairs of univariate features of axial layer 90: (λ1, RA), (I1, Aratio), (I3, RA), etc.

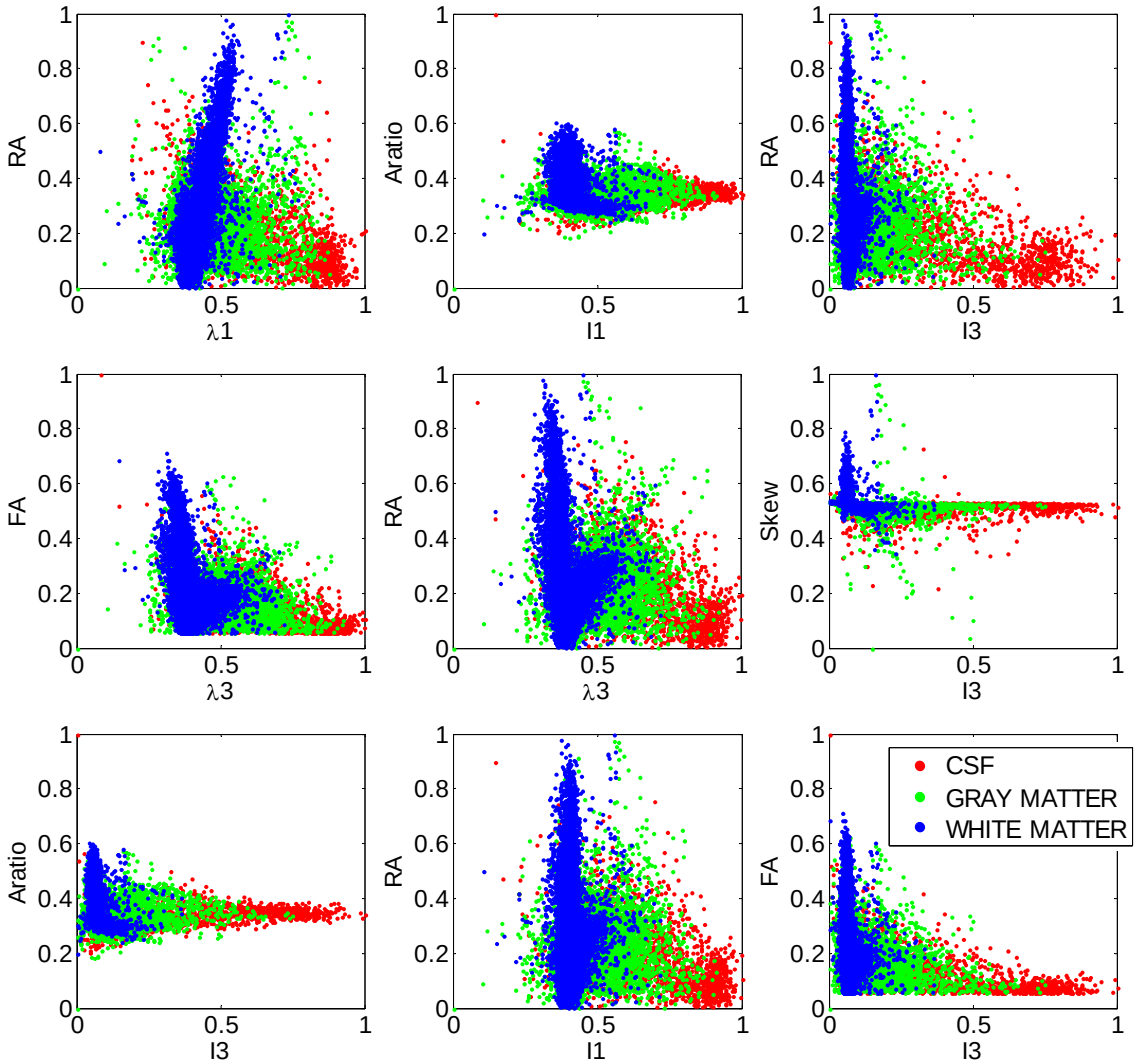


*Figure 6.2: Scatterplots for pairs of univariate features and axial layer #90.*

The scatterplots show that the class-conditional distributions are widely overlapping each other. The feasible pair for WM discrimination is ($\lambda_1$, RA), for GM discrimination is (I1, Aratio), and for CSF discrimination is (I3, RA).

### 6.3.2 Density Functions

Here the distribution of twelve univariate features of axial layer 90 by density functions and joint pdfs, using kernel method (Parzen density estimation) are investigated. Thus it can be visually assessed if some of the features possess a good discrimination power.

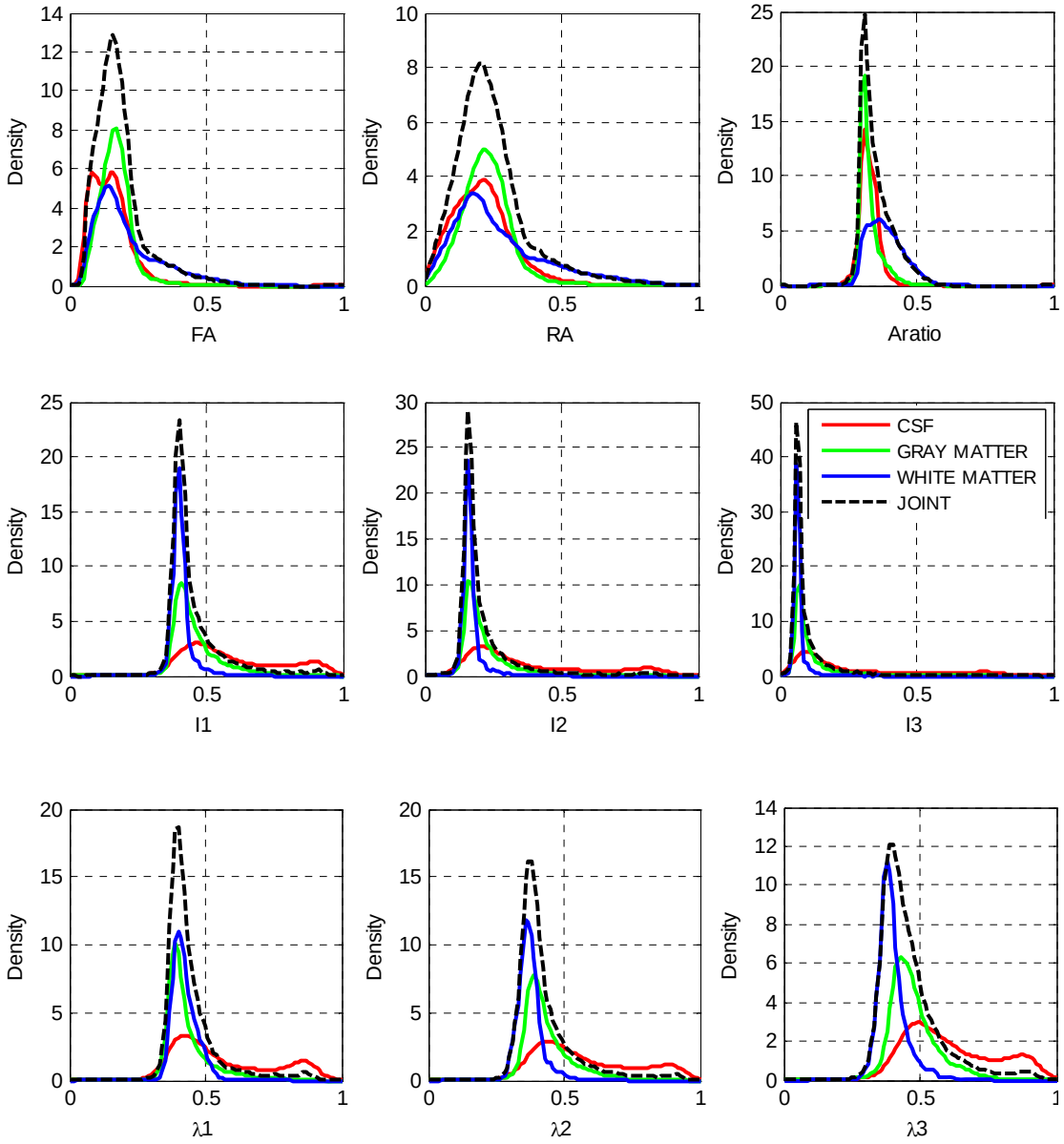


*Figure 6.3: Density functions of CSF (red line), GM (green line), and WM (blue line) plus joint pdf (black dash line) for univariate features, axial layer #90.*

Figure 6.3 shows the tissues are not well separated. This fact was proved by Figure 6.2 as well. Based on the above density functions, appropriate univariate feature for WM discrimination seem to be third eigenvalue ($\lambda_3$), for GM discrimination Aratio, and for CSF discrimination RA.

## 6.4 Real DTI Volume Segmentation

In this section the results of the real DTI volume segmentation are presented. The experiments have been performed on the selected axial layers of the brain volume, using twelve univariate features and twelve feature sets. The segmentation was performed by the modified and standard k-means algorithms with one-step and hierarchical classifiers; and the segmentation performance was evaluated using DSI and AUC measures.

### 6.4.1 Real DTI Data Segmentation based on One-step Classifier

The results of DTI volume segmentation based on one-step classifier are presented below. At first the DSI values and afterward the AUC values of the three-class segmentation are sketched.

#### 6.4.1.1 DSI Values Analysis

The DSI values of the three-class problem, by both modified and standard k-means clustering algorithms using one-step classifier are presented in Figures 6.4 to 6.6.

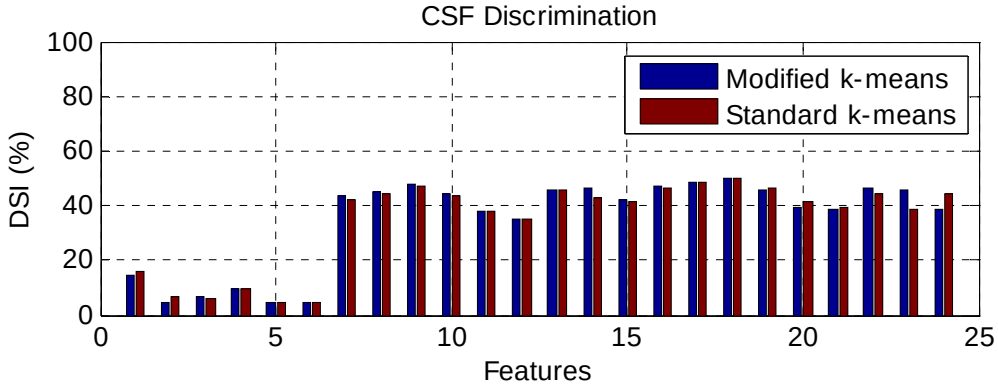


*Figure 6.4: DSI values of 24 feature sets for CSF discrimination by both modified and standard k-means clustering algorithms using one-step classifier method.*

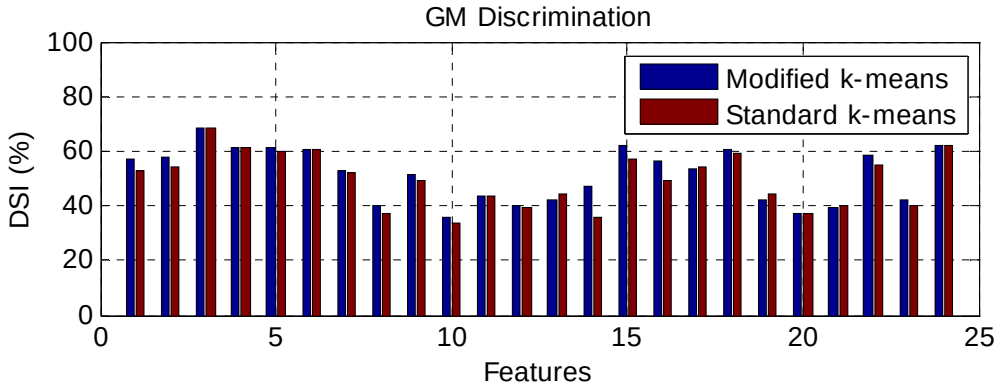


*Figure 6.5: DSI values of 24 feature sets for GM discrimination by both modified and standard k-means clustering algorithms using one-step classifier method.*

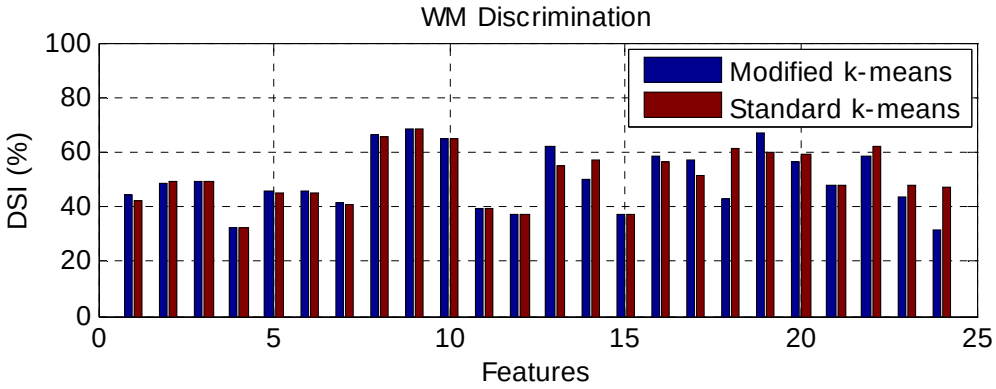


*Figure 6.6: DSI values of 24 feature sets for WM discrimination by both modified and standard k-means clustering algorithms using one-step classifier method.*

The analysis of the Figures 6.4, 6.5, and 6.6 led to the following conclusions:

For CSF discrimination the best DSI value (0.50) was obtained using the feature set 6 (FS6= {FA, RA, $\lambda_3$}) and the modified k-means. For GM discrimination the best DSI value (0.68) was obtained using Aratio feature and the standard k-means. Finally, the best DSI value of the WM discrimination (0.69) was obtained using the third eigenvalue ($\lambda_3$) and modified k-means. The exact values of the DSI values were presented in Appendix I.

### 6.4.1.2 AUC Values Analysis

The total AUC values of three-class problem by both modified and standard k-means clustering algorithms, using one-step classifier are presented in Figure 6.7.

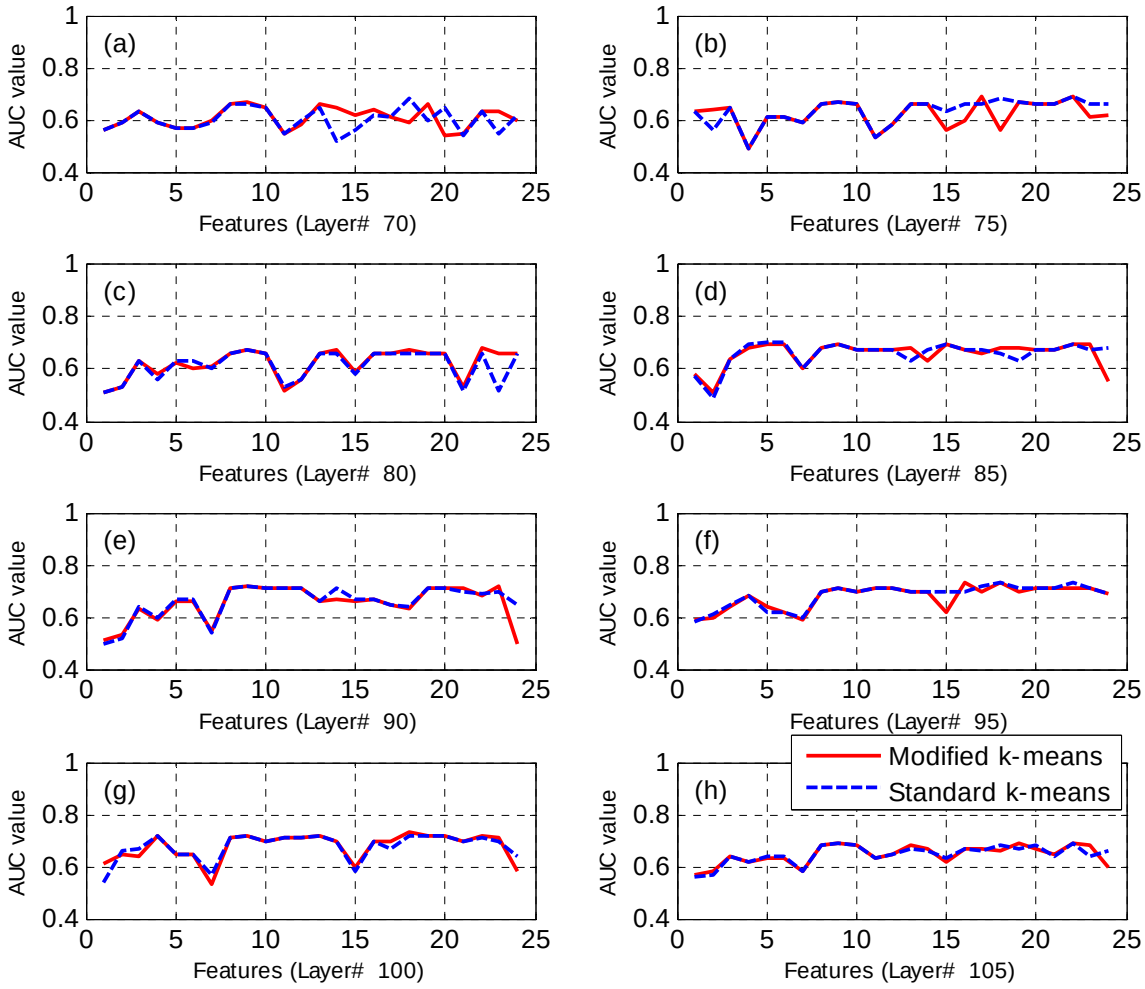


*Figure 6.7: The total AUC value of 3-class problem obtained using modified k-means (red line) and standard k-means (blue dash line). (a-g) AUC values of seven axial layers {70,75,80,85,90,95,100}. (h) the mean AUC of all these layers.*

For both modified and standard k-means, the best AUC value (0.73) was obtained from the feature set 6: FS6= {FA, RA, $\lambda_3$}. Also the best mean AUC value of features (0.67) was obtained from layers 95 and 100. The exact mean AUC values are presented in Appendix II.

### 6.4.2 Real DTI Data Segmentation based on Hierarchical Classifier

The hierarchical classifier (refer to section 5.6) is the second approach for the real DTI-volume segmentation. The DSI values of the segmentation with both modified and standard k-means algorithms are sketched in Figure 6.8.

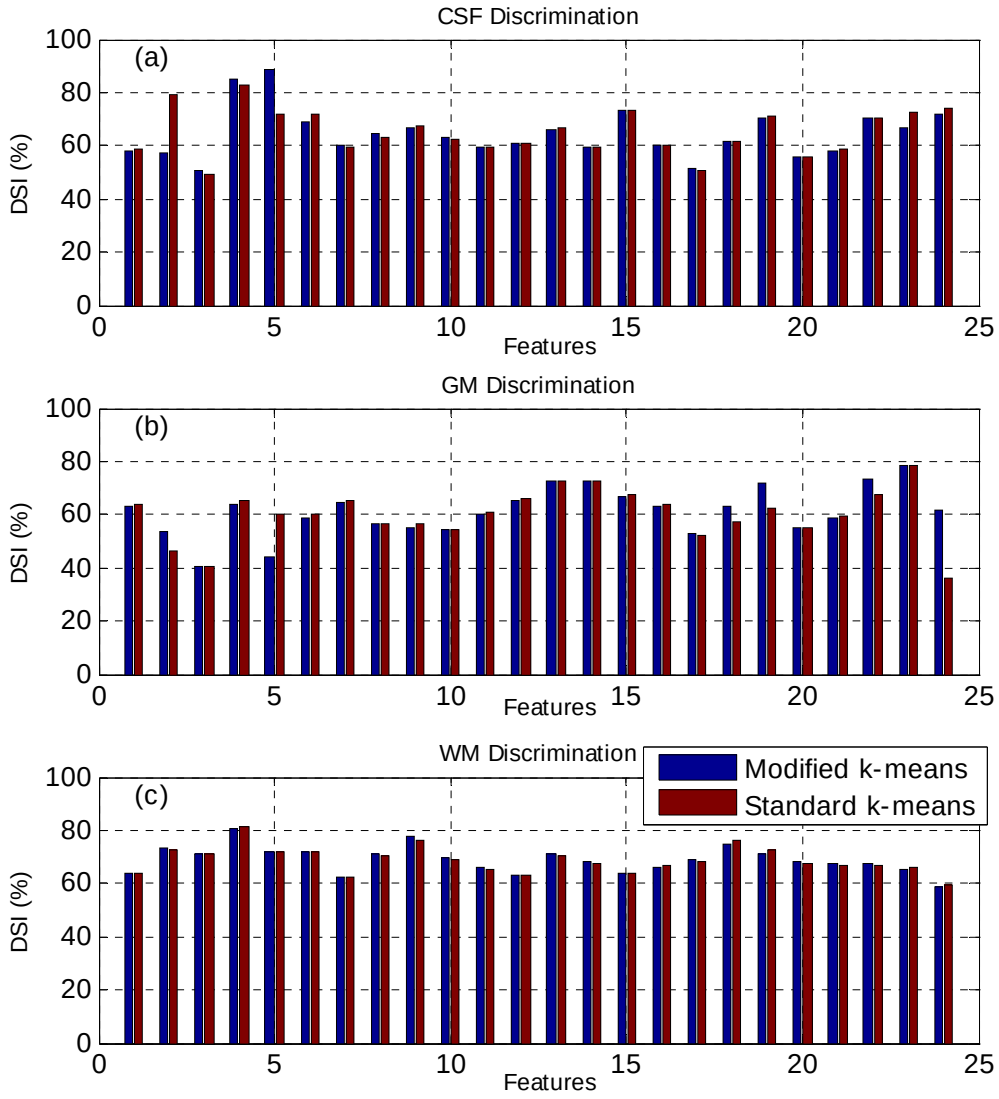


*Figure 6.8: DSI values of segmentation by both modified and standard k-means clustering algorithms using hierarchical classifier on 24 feature sets for these tissues: (a) CSF (b) GM (c) WM.*

The best DSI value for CSF discrimination (0.88) was obtained using the volume ratio (VR) and modified k-means. For GM discrimination, the best DSI value (0.79) was obtained by the standard k-means, using the feature set 10: FS10= {FA, RA, $\lambda_3$, I3}. Finally, the best DSI value of the WM discrimination (0.81) was obtained using the I3 feature and standard k-means (see Appendix III for the exact DSI values).

### 6.4.3 One-step vs. Hierarchical Classifier

To compare the outcomes of the one-step and hierarchical classifiers, the mean DSI values of the CSF, GM, and WM of each feature, for both modified and standard k-means algorithms were calculated. These values were depicted in Figures 6.9 and 6.10. The exact DSI values were presented in Appendix I and Appendix III.

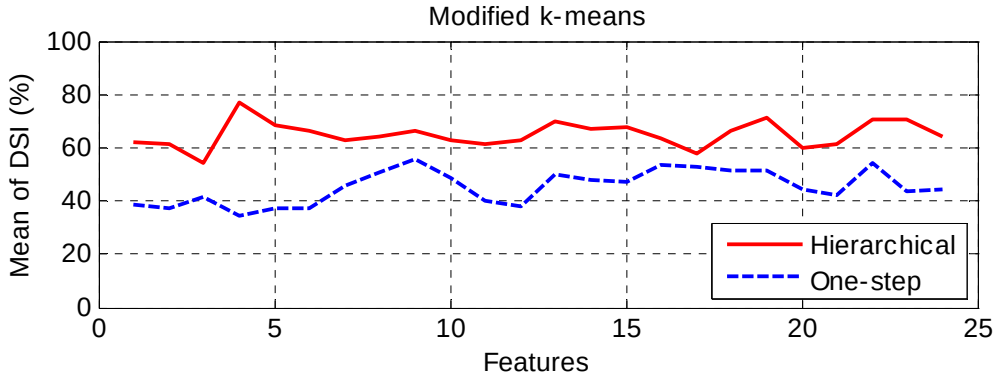


*Figure 6.9: Mean DSI values of 3-class problem by modified k-means using hierarchical and one-step classifiers.*

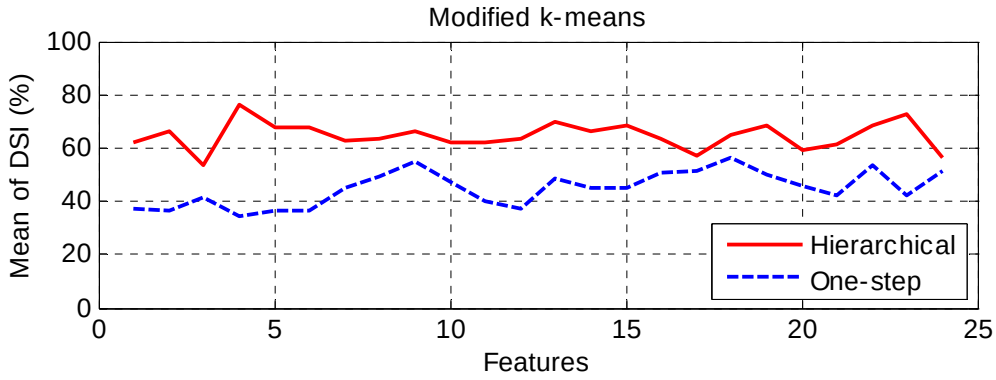


*Figure 6.10: Mean DSI values of 3-class problem by standard k-means using hierarchical and one-step classifiers.*

The most accurate mean DSI value (0.71) was obtained for the hierarchical classifier by modified k-means using feature set 7: FS7= {λ3, Skew, $\lambda_2$, FA, I1}.

## 6.5 Real MRI vs. DTI Data Segmentation

The AUC values of real MR-volume (T1 modality) versus the mean AUC values of the DTI features which have been obtained from segmentation, using one-step classifier, were investigated. Different performance evaluation methods are utilized and presented as follows.

Figure 6.11 shows three-class ROC graphs for T1 data and feature set 4 (FS4= {FA, $\lambda_3$, $\lambda_1$, I2}). For T1 data the WM/non-WM classifier and for FS4 the CSF/non-CSF classifier has the highest AUC value. Total AUC value for T1 data is 0.91 and it is 0.73 for FS4.

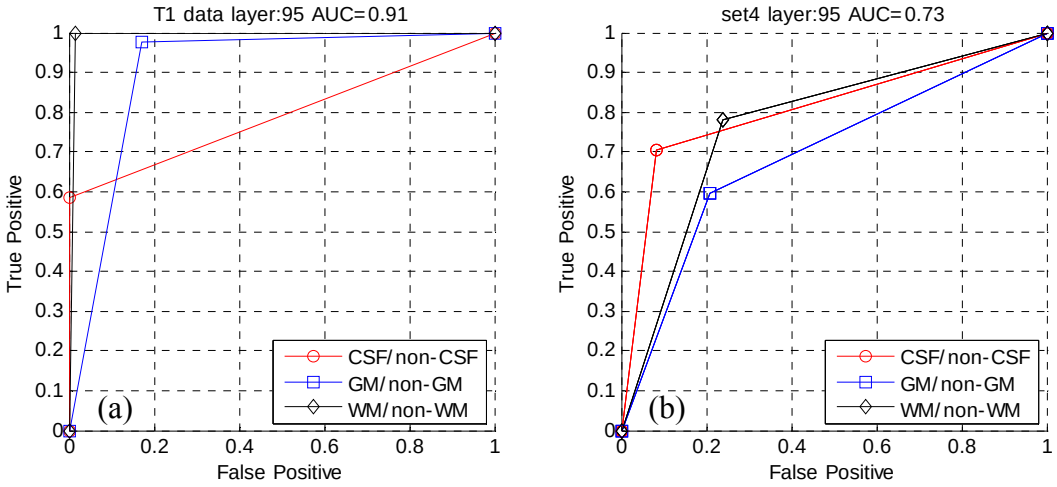


*Figure 6.11: ROC graph of axial layer #95: (a) T1 modality, (b) FS4 feature.*

Table 6.2 shows the mean AUC values of all the features, for each layer for both modified and standard k-means. These results were depicted in Figure 6.12. The best mean AUC value of DTI features (0.67) was obtained from axial layers 95 and 100; also for MR-volume the best AUC value (0.91) was obtained from axial layer 95, for both modified and standard k-means. See Appendix II for the exact AUC values.

*Table 6.2: Mean AUC values of the DTI features and AUC of T1 modality by both modified and standard k-means using one-step classifier of seven layers.*

| Layer# | Modified k-means | | Standard k-means | |
|---|---|---|---|---|
| | DTI | T1 | DTI | T1 |
| 70 | 0.61 | 0.88 | 0.60 | 0.88 |
| 75 | 0.63 | 0.88 | 0.63 | 0.87 |
| 80 | 0.61 | 0.86 | 0.61 | 0.86 |
| 85 | 0.65 | 0.86 | 0.65 | 0.85 |
| 90 | 0.64 | 0.90 | 0.65 | 0.90 |
| 95 | 0.67 | 0.91 | 0.67 | 0.91 |
| 100 | 0.67 | 0.88 | 0.67 | 0.89 |

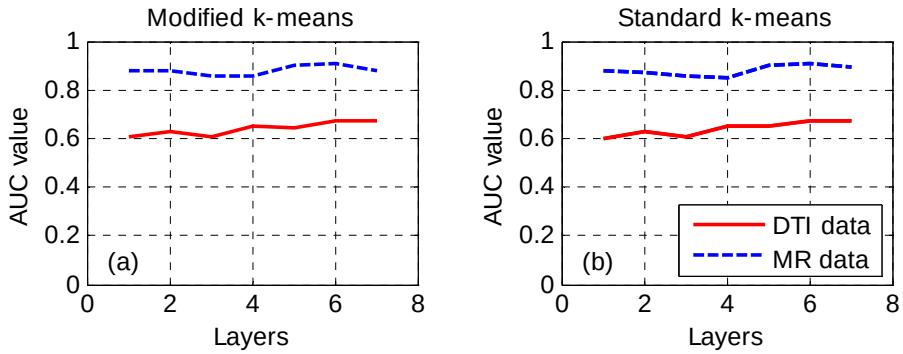


*Figure 6.12: AUC values of one-step classifier on DTI data (red line) and MR data (blue dash line) by (a) Modified k-means, (b) Standard k-means.*

## 6.6 Simulated MRI Data Segmentation

In this section segmentation results of simulated data are presented. Segmentation has been performed on selected axial layers of three MR modalities (T1, T2, PD) and whole T1 brain volume.

### 6.6.1 Selected Layers Segmentation

Here the segmentation results of nine axial layers (35, 40, 75, 80, 85, 90, 95, 100, 145) of T1, T2, and PD modalities by modified k-means with one-step classifier are presented.

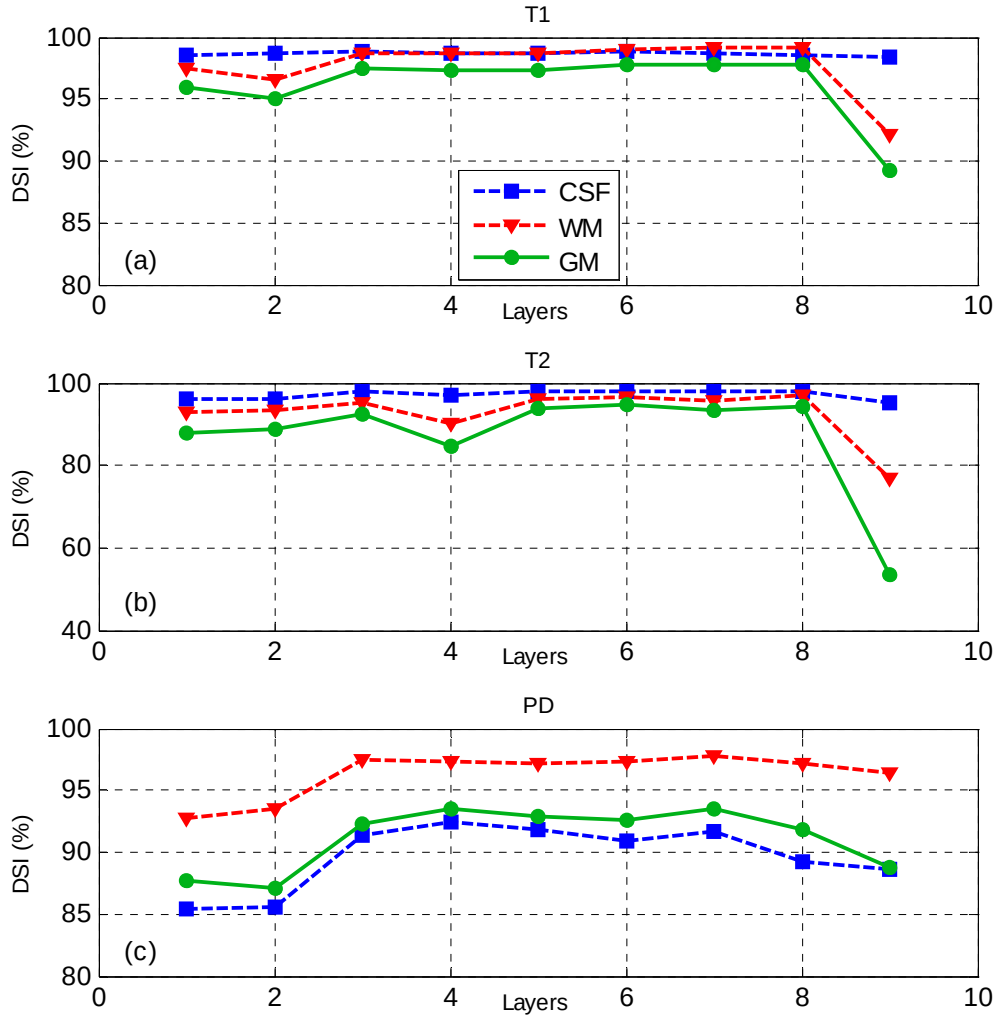


*Figure 6.13: DSI of 3-class segmentation by modified k-means using one-step classifier on nine axial layers (35,40,75,80,85,90,95,100,145) of three modalities: (a) T1 modality, (b) T2 modality, (c) PD modality.*

Figure 6.13 shows, in T1 modality maximum DSI value for CSF is 0.99, for WM is 0.99, and for GM is 0.98. In T2 modality maximum DSI value for CSF is 0.98, for WM is 0.97, and for GM is 0.94. In PD modality maximum DSI value for CSF is 0.92, for WM is 0.98, and for GM is 0.93.

### 6.6.2 Brain Volume Segmentation

Here we present investigation of the accuracy and execution times of both standard and modified k-means algorithms on the whole brain volume, using one-step classifier.

*Table 6.3: DSI and execution time of the segmentation by the modified and standard k-means clustering algorithms on simulated T1 brain volume.*

| Segmentation Algorithm | CSF | GM | WM | Time of Process (Second) |
|---|---|---|---|---|
| Modified k-means | 96.56 | 96.53 | 99.64 | 58.51 |
| Standard k-means | 93.19 | 95.68 | 99.27 | 70.55 |

Table 6.3 shows the execution time of modified k-means is about 1.2 times faster than standard k-means while the DSI values of the discriminated tissues are almost the same for both modified and standard k-means.

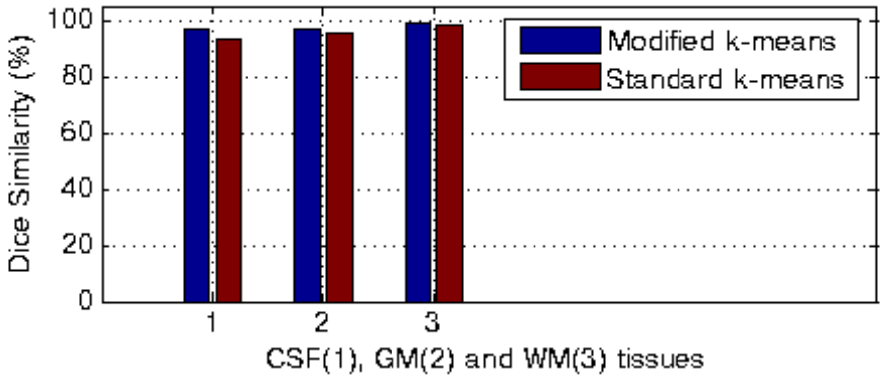


*Figure 6.14: Results of segmentation using simulated T1 modality by the modified and standard k-means using one-step classifier.*

## 6.7 Visualization of Segmentation Results

In this section the WM/non-Wm segmentation results of FA feature and CSF/non-CSF segmentation results of third eigenvalue ($\lambda_3$) are visualized. Also the corresponding CMs are presented for both segmentations.

**Wm/non-WM Segmentation.** The WM/non-Wm segmentation results of FA feature of axial layer 85, are presented below.

Figure 6.15 shows four illustrations of the FA feature (left to right): the original image, ground truth, WM/non-WM segmentation, and detailed segmentation. In the detailed segmentation each region is identified by especial color, WM is cyan, non-WM is yellow, and misclassification is red.

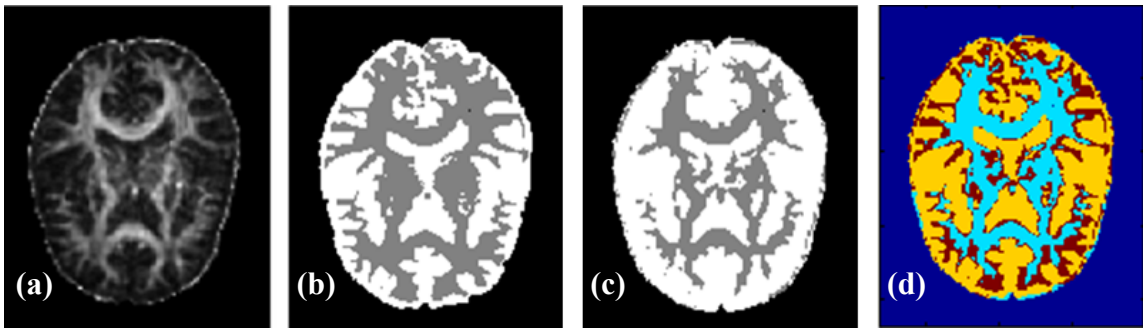


*Figure 6.15: WM/non-WM segmentation of FA feature, axial layer #85,*
*(a) Original FA feature, (b) Ground truth, (c) Segmented feature,*
*(d) Detailed segmentation: WM/cyan; non-WM/Yellow; Misclassification/red.*

The corresponding confusion matrix for the WM/non-WM segmentation is:

$$CM = \begin{bmatrix} 9673 & 633 \\ 141 & 8572 \end{bmatrix}$$

**CSF/non-CSF Segmented.** The CSF/non-CSF segmentation results of third eigenvalue ($\lambda_3$) of axial layer 85 are presented below.

Figure 6.16 shows the segmentation results using the third eigenvalue ($\lambda_3$) (left to right): the original image, ground truth, CSF/non-CSF segmentation, and detailed segmentation. In the detailed segmentation each region is identified by especial color, CSF is cyan, non-CSF is yellow, and misclassification is red.

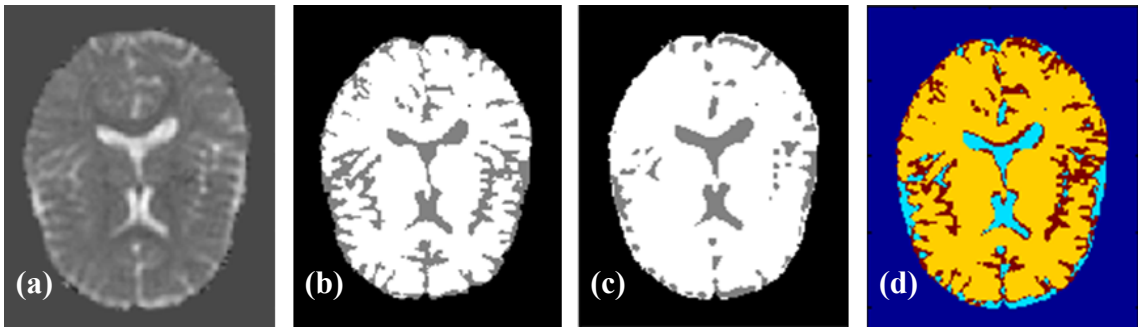


*Figure 6.16: CSF/non-CSF segmentation of $\lambda_3$ feature, axial layer #85,*
*(a) Original $\lambda_3$ feature, (b) Ground truth, (c) Segmented feature,*
*(d) Detailed segmentation: CSF/blue; non-CSF/Yellow; Misclassification/red.*

The CM of the CSF/non-CSF segmentation is:

$$CM = \begin{bmatrix} 5623 & 417 \\ 127 & 2532 \end{bmatrix}$$

## 6.8 Detecting the Stopping criterion for Modified k-means

Figures 6.17 to 6.19 show the experiment for the detection of the suitable stopping value for the modified k-means clustering. In this case the segmentation was done on one axial layer (layer #80) and FA feature.

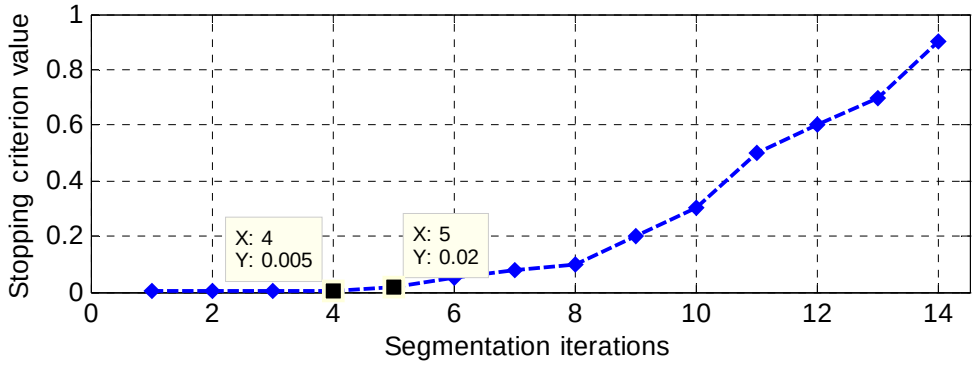


*Figure 6.17: Stopping criterion values, 14 steps in (0,1) interval.*

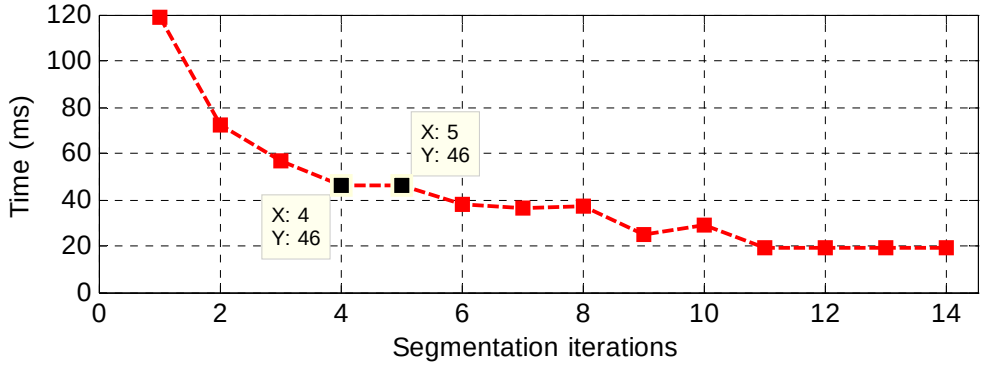


*Figure 6.18: Execution times corresponding to the stopping criterion values in Figure 6.17.*

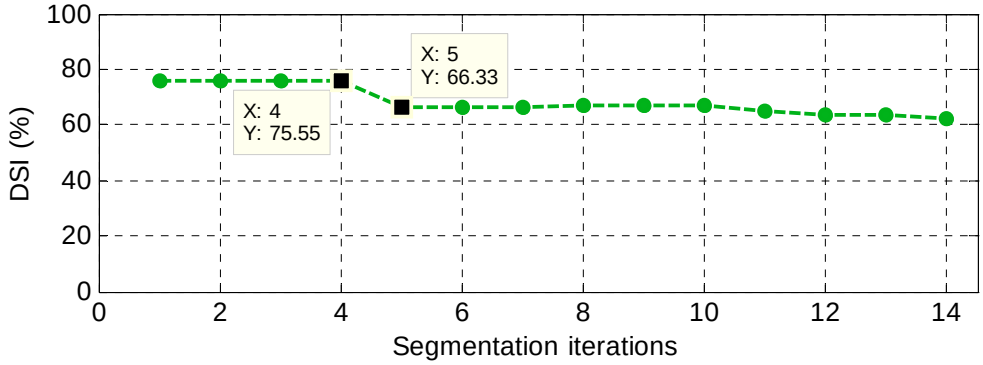


*Figure 6.19: The corresponding DSI values.*

It can be observed that the segmentation performance (DSI value in Figure 6.19) is high for the first four stopping values and then it drops down to a lower value. It means that the segmentation can be done with a higher stopping value and reach the same segmentation accuracy. At the same time the total execution time will be reduced from

ca 120 seconds to ca 45 seconds. In this way, we may reduce the total time which is needed for the segmentation.

## 6.9 Experimental Environment

In this project the segmentation experiments have been performed using the following hardware and software:

**Hardware:**

CPU: P4-2.80 GHz
RAM: 256 MB
Operating system: Windows Vista

**Software:**

MATLAB 2008
FSL 4.1.4
PRTools 4.1

## 6.10 Results comparison

The comparative study result shows common features. Based on different dataset which results slightly bias. Current project results are compared with articles [29] and [30].

**Results of D. Han paper [29]:**
In this paper discriminating the WM and CSF were performed by graph-cuts, FSL-FAST tool, and thresholding method. The results are depicted in comparison with standard and modified k-means in Figure 6.20. It is seen that the WM tissue has been discriminated better than CSF tissue. In addition the best WM discrimination, was obtained by graph-cuts and thresholding method; and for CSF discrimination the best result was obtained by the graph-cuts method.

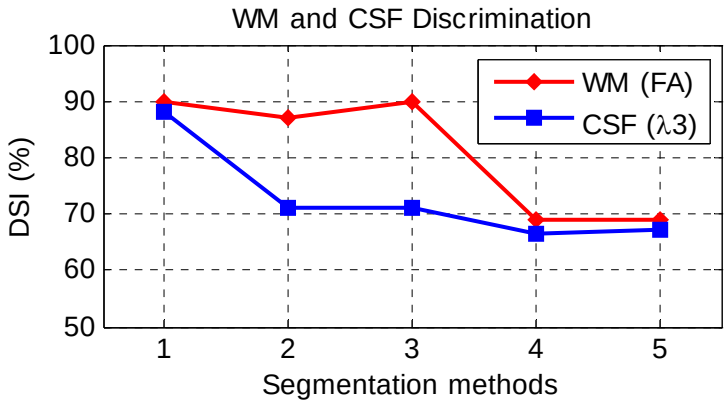


*Figure 6.20: WM and CSF discrimination by five segmentation methods: 1- Graph-cuts, 2- FSL-FAST tool, 3- Thresholding, 4- Modified k-means, 5- Standard k-means; the univariate features are FA and $\lambda_3$.*

**Results of T. Liu paper [30]:**
In this paper the CSF tissue was discriminated by the three eigenvalues ($\lambda_1$,$\lambda_2$,$\lambda_3$). Also the WM tissue was discriminated by FA, RA, and VR. The segmentation was performed by combination of the Hidden Markov Random Field (HMRF) and Expectation-Maximization (EM). The results are depicted in comparison with standard and modified k-mans in Figures 6.21 and 6.22.

Figure 6.21 shows, in CSF discrimination, DSI value of HMRE-EM is lower than that of modified and standard k-means. However, for WM discrimination (see Figure 6.22), DSI value of HMRE-EM is higher than that of modified and standard k-means.

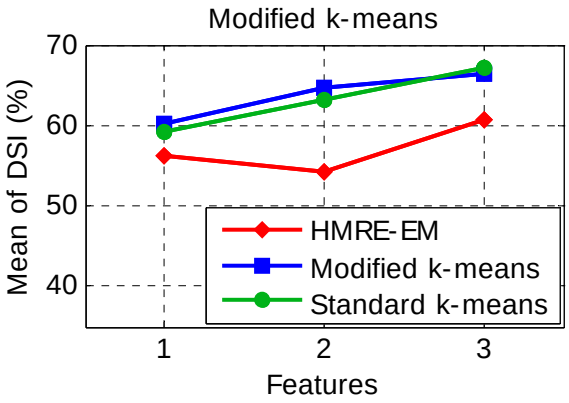


*Figure 6.21: CSF discrimination with three segmentation methods, (features: three eigenvalues $\lambda_1$, $\lambda_2$, $\lambda_3$).*

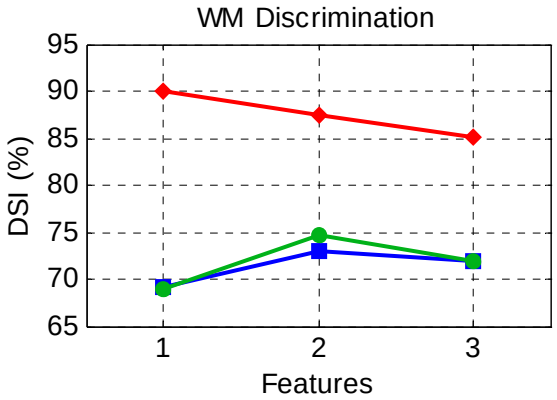


*Figure 6.22: WM discrimination with three segmentation methods, (features: FA, RA, VR).*

# 7 DISCUSSION

The main purpose of this thesis was to develop and investigate methods for brain tissue segmentation using DTI data. Two methods were implemented: standard k-means and modified k-means clustering algorithms. The segmentation was tested using different univariate and multivariate DTI measures.

The analysis of estimated univariate probability density functions showed that the distributions differed from Gaussian shapes and they were not well separated. Also the visual inspection of 2-D feature scatterplots showed that the features overlapped each other and it was difficult to select a good pair of features. This turned out to be inconsistent with the segmentation results' accuracy. The best class separation for the univariate features seemed to be using RA, and for 2-D case using feature pair (I3, RA).

The feature selection led to the enhancement of the total AUC values, for both modified and standard k-means clustering algorithms (see Figure 6.7). The best AUC value (0.73) was obtained for the feature set 6: FS6= {FA, RA, $\lambda_3$}.

The segmentation results for both standard and modified k-means were almost the same, in most of the experiments. Nevertheless, the modified k-means showed higher discrimination on some of the features. However, it cannot be claimed that the modified k-means consistently excels standard k-means on the brain tissue segmentation problems (e.g. see Figures 6.4, 6.5).

Figure 6.9 and Figure 6.10 show that the mean DSI values using hierarchical classifier were higher than those using one-step classifier, for all the features. Therefore, the hierarchical classifier had better discrimination than one-step classifier.

Comparison between the results of DTI-based segmentation and conventional MR-based segmentation showed that the MR data had higher AUC value than DTI data, for both segmentation methods (see Figure 6.12 and Table 6.2).

In case of simulated T1, T2, and PD data, the results indicated that each modality acted differently for different tissues (see Figure 6.13). T1 and T2 modalities gave the best results for CSF discrimination and PD gave the best results for WM discrimination.

The outcome comparison with other articles indicated, the DSI value of WM discrimination in the current project had lower value than that in articles [29] and [30]

(see Figures 6.20 and 6.22). However, DSI value of CSF discrimination in the studied articles had lower value than that in the current project (see Figure 6.21).

In this project many (twenty four) DTI-based features were extracted and investigated. Whereas in the reviewed articles only few features had been considered. This gave a possibility for improvement of the segmentation results. However, this put also a higher demand on a successful feature selection.

# 8 CONCLUSIONS AND FUTURE WORK

## 8.1 Conclusions

In this project DTI data was utilized to discriminate the CSF, GM, and WM tissues in a human brain. For this purpose segmentation has been performed by the standard and modified k-means clustering algorithm. In addition to DTI data, MRI data in three modalities T1, T2, and PD were investigated. The main results are summarized as follows:

- The best segmentation result was obtained using dataset consisting of FA, VR, $\lambda_1$, $\lambda_3$, RA and I3 features.
- The best segmentation results using univariate feature was obtained for feature VR.
- The hierarchical classifier led to higher segmentation accuracy compared to the one-step classifier.
- The WM can be best discriminated using anisotropy features, the GM and CSF tissues can be best discriminated using the largest eigenvalue of the diffusion tensor matrix.
- The feature selection improved the segmentation results, especially for the GM.
- The AUC value for the k-means method and MRI data was larger than using DTI data, which may suggest that DTI does not necessarily leads to improved segmentation accuracy for this segmentation method.
- The modified k-means algorithm led to lower execution time. This was the result of the observation that the k-means iterations can be interrupted after a number of iterations without sacrificing the segmentation accuracy.

In conclusion, the developed algorithm can be used for unsupervised brain tissue segmentation. However, to obtain higher segmentation accuracy a more advanced algorithm that takes into account spatial dependencies might be employed. In addition, a fusion with conventional MR data may be required.

## 8.2 Future Work

The current study has some limitations; in particular only one real subject data and tissue delineation from only one medical expert were accessed. Therefore, the experiments should be repeated on a larger dataset to obtain statistical significance.

Also the segmentation method itself has some shortcomings. For example, the k-means cannot cluster properly non-convex distributions. Other unsupervised clustering methods that can cope with non-convex data and spatial dependencies, e.g. the mean-shift algorithm, could be investigated on this segmentation problem.

In addition, the DTI and MR data have been utilized separately because of the differences in resolution and accuracy. Therefore, investigation on the manner of generating a feature set with combination of DTI and MR data is suggested.

# References


[1] E.D. Angelini, T. Song, B.D. Mensh, and A.F. Laine, “Brain MRI Segmentation with Multiphase Minimal Partitioning: A Comparative Study,” *International Journal of Biomedical Imaging,* vol. 2007, pp. 1-15, 2007.

[2] G. Heckenberg, Y. Xi, Y. Duan, and J. Hua, ”Brain Structure Segmentation from MRI by Geometric Surface Flow,” *International Journal of Biomedical Imaging,* vol. 2006, pp. 1-6, 2006.

[3] O. Commowick, S.K. Warfield, “A Continuous STAPLE for Scalar, Vector, and Tensor Images: An Application to DTI Analysis,” *IEEE Transactions on Medical Imaging,* vol. 28 , pp. 838-846, 2009.

[4] C. Lenglet, M. Rousson, and R. Deriche, "DTI Segmentation by Statistical Surface Evolution", *IEEE Transactions on Medical Imaging,* vol. 25, pp. 685-700, 2006.

[5] S. Mori and P. Van Zijl, “Fiber Tracking: Principles and Strategies - A Technical Review,” *NMR Biomed.,* vol. 15, pp. 468-480, 2002.

[6] L. Concha, D. Gross, and C. Beulieu, “Diffusion Tensor Tractography of The Limbic System,” *Am. J. Neuroradiol.,* vol. 26, pp. 2267-2274, 2005.

[7] M.A. Niznikiewicz, M. Kubicki, and M.E. Shenton, “Recent Structural and Functional Imaging Findings in Schizophrenia," *Current Opinion in Psychiatry,* vol. 16, pp. 123-147, 2003.

[8] S. Zhang, M. Bastin, D.H. Laidlaw, S. Sinha, P.A. Armitage, and T.S. Deisboeck, “Visualization and Analysis of White Matter Structural Asymmetry in Diffusion Tensor MR Imaging Data,” *Magnetic Res. in Med.,* vol. 51, pp. 140-147, 2004.

[9] H. Li, T. Liu, G. Young, L. Guo and S. T. Wong, "Brain tissue segmentation based on DWI/DTI data," in *Biomedical Imaging: Nano to Macro, 2006. 3rd IEEE International Symposium on,* pp. 57-60, 2006.

[10] Mayfield Clinic: http://www.mayfieldclinic.com/PE-AnatBrain.htm, Feb. 01, 2013 [Feb. 10, 2013].

[11] MedlinePlus: www.nlm.nih.gov/medlineplus/ency/imagepages/18117.htm, Jan. 13, 2013 [11, Apr. 2013].

[12] M.D. King, J. Houseman, S.A. Roussel, N. Van Bruggen, S.R. Williams, and D.G. Gadian, “q-Space Imaging of The Brain,” *Magnetic Resonance in Medicine,* vol. 32, pp. 707–713, Dec. 1994.

[13] H. Zhu, D. Xu, A. Raz, X. Hao, H. Zhang, A. Kangarlu, R. Bansal and B. S. Peterson, "A statistical framework for the classification of tensor morphologies in diffusion tensor images," *Magn. Reson. Imaging,* vol. 24, pp. 569-582, 2006.

[14] C.F. Westin, S.E. Maier, H. Mamata, A. Nabavi, F.A. Jolesz, and R. Kikinis, “Processing and Visualization for Diffusion Tensor MRI,” *Medical Image Analysis,* vol. 6, pp. 93-108, June 2002.

[15] D. Lebihan, E. Breton, D. Lallemand, P. Grenier, E. Cabanis, and M. Laval-Jeantet, “MR Imaging of Intravoxel Incoherent Motions: Application to Diffusion and Perfusion in Neurologic Disorders,” *Radiology,* vol. 161, pp.401-407, 1986.

[16] A.L. Alexander, J.E. Lee, M. Lazar, and A.S. Field, “Diffusion Tensor Imaging of The Brain,” *Neurotherapeutics,* vol. 4, pp. 316–329, July 2007.

[17] C. Pierpaoli and P. J. Basser, "Toward a quantitative assessment of diffusion anisotropy," *Magnetic Resonance in Medicine,* vol. 36, pp. 893-906, 1996.

[18] P.J. Basser, J. Mattiello, and D. Lebihan, “MR Diffusion Tensor Spectroscopy and Imaging,” *Biophysical Journal,* vol. 66, pp. 259-267, 1994.

[19] A.L. Alexander, K. Hasan, G. Kindlmann, D.L. Parker, and J.S. Tsuruda, “A Geometric Analysis of Diffusion Tensor Measurements of The Human Brain,” *Magnetic Resonance in Medicine,* vol. 44, pp. 283-291, 2000.

[20] L. Rittner and R. Lotufo, "Diffusion tensor imaging segmentation by watershed transform on tensorial morphological gradient," in *Computer Graphics and Image Processing, 2008. SIBGRAPI'08. XXI Brazilian Symposium on,* pp. 196-203, 2008.

[21] E.M. Akkerman, “Efficient Measurement and Calculation of MR Diffusion Anisotropy Images Using The Platonic Variance Method,” *Magnetic Resonance in Medicine*, vol. 49, pp. 599-604, 2003.

[22] C. Westbrook and C. Roth, “MRI in Practice,” *Pub. Blackwell,* 3rd ed, 2005.

[23] R. Zivadinov, M. Stosic, J.L. Cox, D.P. Ramasamy, M.G. Dwyer, “The Place of Conventional MRI and Newly Emerging MRI Techniques in Monitoring Different Aspects of Treatment Outcome,” *Journal of Neurology,* vol. 255, pp.61-74, 2008.

[24] V.J. Wedeen, RP Wang, J.D. Schmahmann, T. Benner, W.Y. Tseng, G. Dai, D.N. Pandya, P. Hagmann, H. D'Arceuil, A.J. de Crespigny, “Diffusion Spectrum Magnetic Resonance Imaging (DSI) Tractography of Crossing Fibers,” *Journal of Neuroimage,* vol. 41, Issue 4, pp. 1267-77, 2008.

[25] A.J. Taylor, “Diffusion Tensor Imaging: Evaluation of Tractography Algorithm Performance Using Ground Truth Phantom,” *Virginia Polytechnic Institute and State University,* Blacksburg, Virginia, May 2004.

[26] D. Nilsson, “Diffusion Tensor Imaging and Tractography in Epilepsy Surgery Candidates,” *Sahlgrenska Academy at Göteborg University,* Epilepsy Research Group, 2008.

[27] P.L. Bazin, J. Bogovic, D. Reich, J.L. Prince, and D.L. Pham, “Belief Propagation Based Segmentation of White Matter Tracts in DTI,” *Medical Image Computing and Computer-Assisted Intervention (MICCAI),* pp. 943-950, 2009.

[28] X. Cai, Y. Hou, C. Li, J.H. Lee, and W.G. Wee, “Evaluation of Two Segmentation Methods on MRI Brain Tissue Structures,” *28th Annual International Conference of The IEEE EMBS’06,* pp. 3029-3032, 2006.

[29] D. Han, V. Singh, J.E. Lee, E. Zakszewski, N. Adluru, T.R. Oakes, and A. Alexander, "An Experimental Evaluation of Diffusion Tensor Image Segmentation Using Graph-Cuts," *Int. Conf. of The IEEE EMBC,* pp. 5653–5656, 2009.

[30] T. Liu, H. Li, K. Wong, A. Tarokh, L. Guo, and S.T.C. Wong, "Brain Tissue Segmentation Based on DTI Data," *NeuroImage,* vol. 38, pp. 114–123, 2007.

[31] Brainweb: www.med.harvard.edu/AANLIB/home.html, 1999, [Sep. 10, 2012].

[32] NIFTI: http://nifti.nimh.nih.gov, Aug. 12, 2005 [Dec. 10, 2012].

[33] DICOM: http://www.dclunie.com/dicom-status/status.html, Apr. 10, 2013 [Apr. 11, 2013].

[34] MINC: http://en.wikibooks.org/wiki/MINC, Nov. 08, 2011 [Dec. 10, 2012].

[35] Chris Rorden Company: http://www.cabiatl.com/mricro/mricron/dcm2nii.html, May 12, 2007 [Apr. 04, 2013].

[36] FSL Tools: http://fsl.fmrib.ox.ac.uk/fsl/fslwiki/, Sep. 04, 2012 [ Sep. 20, 2012].

[37] S. Aksoy and R. M. Haralick, "Feature Normalization and Likelihood-Based Similarity Measures for Image Retrieval," *Pattern Recognition Letters,* vol. 22, pp. 563–582, April 2001.

[38] L. Ladha and T. Deepa, "Feature Selection Methods and Algorithms," *Int. Journal on Computer Science and Engineering (IJCSE),* vol. 3, pp. 1787-1797, 2011.

[39] R.P.W. Duin, P. Juszczak, P. Paclik, E. Pekalska, D. De-Ridder, D.M.J. Tax, S. Verzakov, PRTools4.1, A Matlab Toolbox for Pattern Recognition, Delft University of Technology, 2007.

[40] R. Maitra, A.D. Peterson, and A.P. Ghosh, "A Systematic Evaluation of Different Methods for Initializing The K-means Clustering Algorithm," *IEEE Trans. on Knowledge and Data Engineering,* vol. 21, pp. 522-534, 2010.

[41] S.S. Khan, "Cluster Center Initialization Algorithm for K-means Clustering," *Pattern Recognition Letters,* NY, USA, vol. 25, Aug. 2004.

[42] P.S. Bradley and U.M. Fayyad, "Refining Initial Points for K-means Clustering," *15th Int. Conf. on Machine Learning. Morgan Kaufmann,* vol. 66, pp. 91-99, 1998.

[43] S.V. Stehman, "Selecting and Interpreting Measures of Thematic Classification Accuracy," *Remote Sensing of Environment,* vol. 62, pp. 77–89, 1997.

[44] S. Miri, N. Passat, and J.P. Armspach, "Topology-Preserving Discrete Deformable Model: Application to Multi-segmentation of Brain MRI," In *Image and Signal Processing,* pp. 67-75, Springer, 2008.

[45] T. Fawcett, "ROC Graphs: Notes and Practical Considerations for Data Mining Researchers," *HP Laboratories Technical Report,* 2003.

[46] M.P. Muller, A.J. McGeer, K. Hassan, J. Marshall, and M. Christian, "Evaluation of Pneumonia Severity and Acute Physiology Scores to Predict ICU Admission and Mortality in Patients Hospitalized for Influenza," *Journal PLoS ONE,* vol. 5, 2010.

# Appendix I

The DSI mean values of seven axial layers: (70, 75, 80, 85, 90, 95, 100) by one-step classifier for both modified and standard k-means clustering algorithms.

| No. | Feature | Modified k-means | | | Standard k-means | | |
|---|---|---|---|---|---|---|---|
| | | CSF | GM | WM | CSF | GM | WM |
| 1 | FA | 14.21 | 56.87 | 44.04 | 15.82 | 52.49 | 42.45 |
| 2 | RA | 4.6 | 57.88 | 48.64 | 6.97 | 54.49 | 48.98 |
| 3 | Aratio | 6.62 | 68.26 | 49.21 | 6.3 | 68.54 | 49.53 |
| 4 | Skew | 9.57 | 61.53 | 32.1 | 9.35 | 61.24 | 32 |
| 5 | VR | 4.58 | 61.24 | 45.45 | 4.54 | 60.28 | 44.97 |
| 6 | VF | 4.73 | 60.72 | 45.8 | 4.56 | 60.32 | 44.96 |
| 7 | $\lambda_1$ | 43.59 | 53.03 | 41.61 | 42.35 | 52.28 | 40.74 |
| 8 | $\lambda_2$ | 45.21 | 40.12 | 66.12 | 44.03 | 37.47 | 65.69 |
| 9 | $\lambda_3$ | 47.93 | 51.4 | 68.68 | 47.09 | 49.52 | 68.36 |
| 10 | I1 | 44.61 | 35.5 | 65.18 | 43.53 | 33.7 | 64.84 |
| 11 | I2 | 37.92 | 43.89 | 39.3 | 37.68 | 43.43 | 39.16 |
| 12 | I3 | 35.16 | 40.37 | 37.56 | 34.78 | 39.59 | 37.39 |
| 13 | FS1 | 45.58 | 42.13 | 62.08 | 45.91 | 44.17 | 54.64 |
| 14 | FS2 | 46.23 | 47.01 | 50.3 | 42.8 | 36.13 | 57.1 |
| 15 | FS3 | 42.45 | 62.05 | 37.12 | 41.6 | 57.1 | 37.25 |
| 16 | FS4 | 47.06 | 56.15 | 58.16 | 46.24 | 49.11 | 56.45 |
| 17 | FS5 | 48.93 | 53.66 | 56.74 | 48.28 | 54.57 | 51.48 |
| 18 | FS6 | 50.21 | 60.93 | 42.88 | 49.89 | 58.87 | 61.16 |
| 19 | FS7 | 45.52 | 41.9 | 66.72 | 46.2 | 44.2 | 59.71 |
| 20 | FS8 | 39.47 | 37.35 | 56.28 | 41.51 | 37.23 | 59.41 |
| 21 | FS9 | 38.88 | 39.58 | 47.87 | 39.26 | 40.02 | 48.03 |
| 22 | FS10 | 46.72 | 58.53 | 58.39 | 44.65 | 54.87 | 62.07 |
| 23 | FS11 | 45.81 | 42.41 | 43.53 | 39 | 40.14 | 48.02 |
| 24 | FS12 | 38.39 | 62.2 | 31.38 | 44.41 | 61.77 | 47.36 |

# Appendix II

The mean AUC values of seven axial layers: (70, 75, 80, 85, 90, 95, 100) by modified and standard k-means clustering algorithms using one-step method classifier.

| No. | Feature | Modified k-means | Standard k-means |
|---|---|---|---|
| | | Mean AUC | Mean AUC |
| 1 | FA | 0.57 | 0.56 |
| 2 | RA | 0.58 | 0.57 |
| 3 | Aratio | 0.64 | 0.64 |
| 4 | Skew | 0.62 | 0.62 |
| 5 | VR | 0.63 | 0.64 |
| 6 | VF | 0.63 | 0.64 |
| 7 | $\lambda_1$ | 0.58 | 0.58 |
| 8 | $\lambda_2$ | 0.68 | 0.68 |
| 9 | $\lambda_3$ | 0.69 | 0.69 |
| 10 | I1 | 0.68 | 0.68 |
| 11 | I2 | 0.63 | 0.63 |
| 12 | I3 | 0.65 | 0.65 |
| 13 | FS1 | 0.68 | 0.67 |
| 14 | FS2 | 0.67 | 0.66 |
| 15 | FS3 | 0.62 | 0.63 |
| 16 | FS4 | 0.67 | 0.67 |
| 17 | FS5 | 0.67 | 0.66 |
| 18 | FS6 | 0.66 | 0.68 |
| 19 | FS7 | 0.69 | 0.67 |
| 20 | FS8 | 0.67 | 0.68 |
| 21 | FS9 | 0.65 | 0.64 |
| 22 | FS10 | 0.69 | 0.69 |
| 23 | FS11 | 0.68 | 0.64 |
| 24 | FS12 | 0.60 | 0.66 |

# Appendix III

The DSI mean values of seven axial layers: (70, 75, 80, 85, 90, 95, 100) by hierarchical classifier for both modified and standard k-means clustering algorithms.

| No. | Feature | Modified k-means | | | Standard k-means | | |
|---|---|---|---|---|---|---|---|
| | | CSF | GM | WM | CSF | GM | WM |
| 1 | FA | 58.21 | 63 | 64.19 | 58.93 | 63.89 | 63.97 |
| 2 | RA | 57.34 | 53.64 | 73.01 | 79.51 | 46.11 | 72.82 |
| 3 | Aratio | 50.49 | 40.53 | 71.36 | 49.23 | 40.65 | 70.93 |
| 4 | Skew | 85.31 | 63.93 | 80.94 | 82.76 | 64.99 | 81.49 |
| 5 | VR | 88.57 | 44.21 | 71.89 | 71.87 | 60.25 | 71.96 |
| 6 | VF | 68.92 | 58.83 | 71.96 | 71.87 | 60.25 | 71.96 |
| 7 | $\lambda_1$ | 60.1 | 64.87 | 62.58 | 59.26 | 65.56 | 62.45 |
| 8 | $\lambda_2$ | 64.54 | 56.59 | 71.07 | 63.26 | 56.21 | 70.18 |
| 9 | $\lambda_3$ | 66.49 | 55.36 | 77.85 | 67.18 | 56.24 | 76.25 |
| 10 | I1 | 63.26 | 54.33 | 69.87 | 62.56 | 54.51 | 69.17 |
| 11 | I2 | 59.16 | 59.92 | 65.86 | 59.29 | 60.6 | 65.36 |
| 12 | I3 | 60.86 | 65.2 | 63.1 | 60.94 | 65.74 | 62.78 |
| 13 | FS1 | 66.42 | 72.47 | 71.49 | 67.11 | 72.84 | 70.56 |
| 14 | FS2 | 59.34 | 72.9 | 68.12 | 59.25 | 72.84 | 67.86 |
| 15 | FS3 | 73.15 | 66.92 | 63.95 | 73.35 | 67.19 | 63.77 |
| 16 | FS4 | 60.05 | 63.27 | 66.22 | 60.55 | 63.59 | 66.91 |
| 17 | FS5 | 51.17 | 52.72 | 69.18 | 50.75 | 52.43 | 68.22 |
| 18 | FS6 | 61.61 | 63.46 | 74.64 | 61.5 | 57.23 | 76.12 |
| 19 | FS7 | 70.68 | 72.13 | 71.39 | 71.07 | 62.48 | 72.33 |
| 20 | FS8 | 55.52 | 55.01 | 68.56 | 55.49 | 54.99 | 67.73 |
| 21 | FS9 | 58.21 | 59.12 | 67.16 | 58.44 | 59.73 | 66.45 |
| 22 | FS10 | 70.22 | 73.15 | 67.45 | 70.36 | 67.68 | 66.48 |
| 23 | FS11 | 66.97 | 78.58 | 65.35 | 72.39 | 78.64 | 66.29 |
| 24 | FS12 | 71.6 | 61.33 | 58.89 | 74.16 | 36.35 | 59.17 |